A striatal circuit balances learned fear in the presence and absence of sensory cues

Michael Kintscher[1], Olexiy Kochubey[1], Ralf Schneggenburger[1*]

[1] Laboratory for Synaptic Mechanisms, Brain Mind Institute, School of Life Science, Ecole Polytechnique Fédérale de Lausanne (EPFL), Switzerland.

* Corresponding author; e-mail ralf.schneggenburger@epfl.ch

Summary

During fear learning, defensive behaviors need to be finely balanced, to allow animals to return to normal behaviors after the termination of threat-indicating sensory cues. Nevertheless, the circuits underlying such balancing are largely unknown. Here, we investigate the role of direct (D1R+) - and indirect (Adora+) pathway neurons of the amygdala-striatal transition zone (AStria) in fear learning. *In-vivo* Ca^{2+} imaging revealed that fear learning increased the responses of D1R+ AStria neurons to an auditory CS, given that the animal moved. In Adora+ neurons, fear learning also induced a differential activity during freezing and movement, albeit with little influence of the CS. *In-vivo* optogenetic silencing during the training day showed that plasticity in D1R+ AStria neurons contributes to auditory-cued fear memories, whereas Adora+ neurons suppressed learned freezing when no CS was present. Circuit tracing experiments identified cortical input structures to the AStria, and recording of optogenetically-evoked EPSCs at the corresponding projection revealed different forms of long-term plasticity at synapses onto D1R+ and Adora+ AStria neurons. Taken together, direct- and indirect pathways neurons of the AStria show differential signs of *in-vivo* and *ex-vivo* plasticity after fear learning, and balance defensive behaviors in the presence and absence of aversively motivated sensory cues.

Introduction

Fear learning is an evolutionary conserved behavior, critically important for animals to detect signs of threats in an ever-changing environment (Phelps and LeDoux, 2005; Janak and Tye, 2015). As such, fear learning is relevant for the survival of animals. Nevertheless, learned defensive behaviors need to be finely balanced, so that animals can return to their normal behaviours after cessation of threat-indicating sensory cues allows (Zanette et al., 2011). Furthermore, a pathological overexpression of defensive behaviours is a hallmark of several anxiety-related disorders in humans (Dunsmoor et al., 2011). Therefore, it is important to understand the neuronal circuits that balance the expression of learned defensive behaviors during and after the presence of threat-predicting sensory cues.

The study of the neuronal mechanisms of fear learning has been strongly facilitated by employing auditory-cued fear learning in model animals like rodents (Davis, 1992; LeDoux, 2000). In fear learning, subjects learn to associate an initially neutral auditory cue, the conditioned stimulus (CS), with an aversive or painful outcome like a footshock (the unconditioned stimulus, US). After associative learning, an animal will develop a defensive behavior when the CS is later presented alone (Fanselow, 2018). The defensive behavior that is mostly studied in the context of fear learning in rodents is behavioral arrest, also called freezing (Fanselow, 1994). Studies spanning several decades have firmly established that the amygdala has an important role in fear learning (see Davis, 1992; LeDoux, 2000; Duvarci and Paré, 2014; Tovote et al., 2015, for reviews). In the lateral (LA)- and basal amygdala (LA and BA respectively), auditory (CS) and somatosensory (US) information are integrated (Romanski et al., 1993; Quirk et al., 1995; Amano et al., 2011; Grewe et al., 2017), while the execution of learned freezing depends on a central amygdala to midbrain (periaqueductal gray) projection (LeDoux et al., 1988; Tovote et al., 2016). Nevertheless, given that freezing is a strong change in the behavioral pattern of an animal, it is likely that further neuronal circuits beyond the BLA - central amygdala - midbrain axis are involved in fear learning.

The striatum is part of the basal ganglia motor system, a neuronal system with important roles in movement regulation (for reviews, see Hikosaka et al., 2000; Graybiel, 2005; Grillner et al., 2005; Redgrave et al., 2010; Nelson and Kreitzer, 2014; Klaus et al., 2019). The principal neurons of the striatum are inhibitory projection neurons of two types: First, striato-nigral neurons that project in a direct pathway to output structures like the Substantia nigra pars reticularis (SNR) and others; these neurons selectively express D1-dopamine receptors. Second, striato-pallidal neurons which project in a more indirect pathway towards the basal ganglia output structures; these neurons selectively express D2-dopamine receptors, and also adenosine-2A receptors (Adora) (Gerfen et al., 1990; Schiffmann and Vanderhaeghen, 1993). Different sub-areas of the striatum have different roles in motor control and motor learning. The dorsal striatum is involved in the learning of motor sequences and in the selection of appropriate actions (Nelson and Kreitzer, 2014; Klaus et al., 2019), as well as in habit formation (Redgrave et al., 2010; Burguiere et al., 2015). The ventral striatum is implicated in reward-based learning (Humphries and Prescott, 2010; Cox and Witten, 2019). Recently, based on a systematic study of the cortical inputs to the mouse striatum, a further sub-area of the striatum was identified; a posterior area called tail striatum (Hintiryan et al., 2016; Hunnicutt et al., 2016). Interestingly, early *in-vivo* recordings in the LA have found US-responsive neurons also in the amygdala - striatal transition zone (AStria; Romanski et al., 1993). The AStria is adjacent to the LA and part of the tail striatum, and is similarly composed of D1R-expressing (DR1+) and D2R- and adenosine-2A-receptor expressing (Adora+) neurons (Gangarossa et al., 2019). Nevertheless, a possible role of the AStria in fear learning has not been explored in a systematic fashion.

Here, we use *in-vivo* miniature microscope Ca^{2+} imaging, as well as *in-vivo* and *ex-vivo* optogenetic approaches and circuit tracing, to investigate the role of the two subtypes of AStria neurons in auditory-cued fear learning.

Results

Fear learning causes interdependent coding for tones and movement in D1R+ AStria neurons

The AStria has been known to respond to auditory- and footshock stimulation (Romanski et al., 1993), and the tail striatum, which partially overlaps with the AStria, is innervated by dopamine axons which code for salient sensory stimuli (Menegas et al., 2018). Nevertheless, the *in-vivo* activity of AStria principal neurons themselves, and a possible role of this structure in fear learning, are unknown. We started by recording the activity of AStria neurons during a three-day fear learning paradigm (Figure 1A). To access the AStria, a brain area deeply nested in the posterior-ventral striatum close to the basolateral - and central nuclei of the amygdala, we used miniature-microscope Ca^{2+} imaging (Figure 1B, C; Ghosh et al., 2011). The AStria, similar to other striatal circuits, contains D1-receptor expressing neurons, and D2-receptor, or Adora (adenosine2A-receptor)-expressing neurons (Gerfen et al., 1990; Gangarossa et al., 2019). Therefore, we used either $D1R^{Cre}$, or $Adora^{Cre}$ mice, to unambiguously and separately target the expression of GCamp6m to each subpopulation of AStria neurons, combined with a Cre-dependent AAV vector (Fig. 1B; Materials and Methods). In a first series of experiments (Figure 1, 2), D1R+ AStria neurons were continuously imaged during each day of the fear learning protocol (day 1 - habituation; day 2 - training; day 3 - retrieval).

D1R+ AStria neurons showed, in general, a low frequency of Ca^{2+} events, especially on the habituation day (~ 0.01 – 0.02 Hz average frequency across the population; Figure 1D; see also Figure 2T). On the habituation day of the fear learning protocol, 30-s CS stimulation blocks consisting of 7 kHz tone beeps were applied (0.1s duration, repeated 30 times at 1 Hz; see Figure 1, Figure Suppl. 1 for the fear learning protocol). To this auditory stimulation, some D1R+ neurons responded, albeit with a low response fidelity (Figure 1D). During the training day, when each of the six CS blocks was followed by a 1-s footshock, many D1R+ AStria neurons robustly responded

110 to the footshocks (Figure 1E, G, H). During the fear memory retrieval day, when the CS was
111 presented alone in a different context, the activity of D1R+ AStria neurons seemed to increase
112 during the CS presentation (Figure 1F).
113
114 We performed a deconvolution analysis to derive the action potential (AP) activity of AStria
115 neurons, taking into account the timing and amplitude of individual Ca^{2+} events (Yaksi and
116 Friedrich, 2006). We then constructed peri-stimulus time histograms (PSTHs) and analyzed the
117 significance of the responses with receiver-operated characteristic analysis (ROC; Britten et al.,
118 1992); see Materials and Methods). About one-third of the imaged D1R+ AStria neurons showed a
119 significant footshock response on day 2 (Figure 1G, H; ROC; see horizontal dashed line; 57 out of
120 167 neurons). Regarding the responses to individual tone beeps, the tone-driven activity of the most
121 active D1R+ AStria neurons was clearly time-locked (see one example neuron in Figure 1I). ROC
122 analysis showed that the number of neurons with a significant response to tones increased on day 2,
123 and further increased on day 3 (Figure 1J, K; $p = 0.0001$, Chi^2 test for trend; 184, 167 and 193
124 neurons were imaged on days 1, 2, 3, respectively; N = 8 $D1R^{Cre}$ mice). Averaging the PSTHs over
125 all imaged neurons similarly suggested an increased tone response in the population of D1R+
126 neurons during fear learning (Figure 1L). Thus, *in-vivo* Ca^{2+} imaging showed that a significant
127 fraction of D1R+ neurons in the AStria responds to footshocks, and furthermore, that D1R+
128 neurons increase their responsiveness to the CS.
129
130 During fear learning, rodents acquire a defensive behavior in response to a CS, in the form of
131 freezing (LeDoux, 2000; Fanselow, 2018). In our experiments, freezing bouts of mice typically
132 lasted a few seconds, and were interrupted by movement re-initiation (see e.g. Figure 1 D-F).
133 Interestingly, visual inspection of Ca^{2+} population data suggested that D1R+ AStria neurons were
134 preferentially active during the CS blocks, and within these at times when the animal moved (see
135 e.g. Figure 1F). We therefore first asked whether during the CS, transitions from freezing to

136 movement would drive activity in D1R+ AStria neurons. PSTHs of the Ca^{2+} - events using the
137 movement onset for the alignment revealed Ca^{2+} events in response to movement onset in a
138 subpopulation of D1R+ AStria neurons, as analyzed during the CS epochs (Figure 1M; called
139 "movement-ON" responses). ROC analysis showed that a significant movement-ON response was
140 present in ~ 5% of the neurons on the habituation day; the percentage of responding neurons
141 increased to ~ 20% on day 2 and 3 of the fear learning protocol (Figure 1M, N; $p = 0.003$; Chi-
142 square test for trend). The average PSTH for the entire population of imaged D1R+ neurons also
143 indicated a stronger population Ca^{2+} response during day 2 and day 3 as compared to day 1 (Figure
144 1O). The response fidelity of individual neurons to movement onset showed a highly skewed
145 distribution, with significantly more non-zero values during the training day and the fear memory
146 retrieval day (Figure 1P, $p < 0.0001$, Kruskal-Wallis [KW] test followed by Dunn's multiple
147 comparisons [MC] test; Hab vs. Train, $p = 0.0002$; Hab vs. Ret, $p < 0.0001$). The estimated AP
148 content, derived from the amplitude of the Ca^{2+} events (see Materials and Methods), was changed
149 less substantially (Figure 1Q, $p = 0.0159$, KW test followed by Dunn's MC test; Train vs. Ret, $p =$
150 0.0155). We next analyzed the movement-ON responses in the absence of the CS, and found that
151 these were substantially smaller than during the CS (Figure 1R, and Figure 1, Figure Suppl. 2).
152 Finally, when we aligned the Ca^{2+} event traces to *freezing* onset, we found a decreased Ca^{2+} event
153 frequency (Figure 1, Figure Suppl. 3, 4). These experiments thus show that D1R+ AStria neurons
154 increase their AP firing activity during the onset of movements after a period of immobility.
155 Furthermore, the movement-ON responses were more pronounced during the CS than in the
156 absence of a tone, and fear learning causes an increase in the number of D1R+ AStria neurons
157 which showed movement-ON responses during the CS.
158
159 These results indicate that the representation of movement-ON transitions, and the coding for
160 sensory events (tones) in the AStria positively influence each other. We therefore next validated
161 whether the tone responses, which we had analyzed above irrespective of movement state (Figure

162 1I-L), would depend in their intensity on the latter. This analysis showed that during fear retrieval,
163 the response fidelity to tone beeps was significantly higher during movement than during freezing
164 (Figure 1S, left, $p < 0.0001$, KW test followed by Dunn's MC test; Hab_Frz vs Hab_Move, $p <$
165 0.0001; Train_Frz vs Train_Move, $p = 0.0004$; Ret_Frz vs Ret_Move, $p = 0.0027$). Furthermore,
166 the estimated AP content of the Ca^{2+} events was significantly higher during movement than during
167 freezing (Figure 1S; $p = 0.0012$, KW test followed by Dunn's MC test; Train_Frz vs Train_Move, p
168 $= 0.0007$). Therefore, similarly to the movement-ON responses which were potentiated by the
169 presence of the CS, the response to auditory stimuli during the CS were potentiated during
170 movement as compared to freezing. These results thus reveal an inter-dependency of CS-driven
171 responses, and movement driven responses of D1R+ AStria neurons.
172
173 For a more comprehensive analysis of how the Ca^{2+}-event frequency depends on the movement
174 state of the animal *and* on the presence or absence of a CS, we analyzed the average Ca^{2+} event
175 frequency for the four combinations of movement states / tone presentations, for each day of the
176 fear conditioning paradigm (Figure 1T). The data was significantly different across conditions ($p <$
177 0.0001; KW test). Pairwise comparisons showed that during day 1 (habituation), tones did not
178 change the activity of D1R+ during the movement state (Dunn's MC test; Mov_noCS_Hab vs.
179 Mov_CS_Hab, $p = 0.286$); we did not statistically compare the data involving the freezing state
180 because of a paucity of freezing events on the habituation day.. On days 2 and days 3 of the fear
181 learning paradigm, this pattern of activity of D1R+ neurons profoundly changed (Figure 1T). Thus,
182 the CS now induced a significant *increase* of activity in D1R+ neurons *given* that the animals
183 moved (Dunn's MC test; Mov_noCS_Train vs. Mov_CS_Train, $p = 0.0008$), whereas in the
184 freezing state, the CS induced a *decreased* activity (Dunn's MC test; Frz_noCS_Train vs.
185 Frz_CS_Train, $p = 0.0001$). As a consequence, during the CS, the activity of D1R+ neurons was
186 significantly higher when the mice moved, as compared to when they froze (~ 2.5 fold increase;
187 Dunn's MC test; Frz_CS_Train vs. Mov_CS_Train, $p < 0.0001$), whereas the activity was

188 unchanged between movement and freezing state in the absence of a CS (Dunn's MC test,
189 Frz_noCS_Train vs Mov_noCS_Train, $p = 0.99$). This activity pattern was maintained during the
190 fear memory retrieval day (day 3), when again the CS increased the activity of D1R+ neurons *given*
191 that the mice moved (Dunn's MC test; Mov_noCS_Ret vs. Mov_CS_Ret, $p = 0.013$), and the CS
192 *decreased* their activity given that the mice froze (Dunn's MC test; Frz_noCS_Ret vs. Frz_CS_Ret;
193 $p < 0.0001$). Thus, the activity of the D1R+ AStria neurons, during and after fear learning, is
194 strongly increased when two conditions are met: Movement, and the presence of an aversively-
195 motivated sensory cue.
196
197 To determine the location of the imaged neurons and to compare them across mice, we semi-
198 automatically aligned the center of the GRIN lens to a mouse brain atlas in each mouse, and
199 generated a common cell map based on the cell coordinates relative to the lens center (Materials
200 and Methods). This revealed a hotspot of footshock- and tone-responding D1R+ neurons in the
201 posterior - ventral region of the tail striatum medial to the LA (Figure 2A, B). D1R+ neurons with
202 movement-ON responses (as measured during the retrieval day) were located in roughly the similar
203 area, and were in addition found in more anterior regions (~ -1.0 mm AP; see Figure 2C). An
204 analysis of the overlap of neurons with the various types of responses showed that on the
205 habituation day, neurons with responses to the CS, and to movement did not strongly overlap, and
206 represented only a small proportion of the imaged neurons on this day (Figure 2D). During the
207 training day of the fear learning protocol, the neurons with movement-ON responses increased in
208 numbers and substantially overlapped with a larger sub-population of footshock-responsive
209 neurons. On the retrieval day, the populations of both tone- and movement responders had
210 increased, and their overlap became more substantial as compared to the habituation day (Figure
211 2D). Taken together, *in-vivo* Ca^{2+} imaging with a miniature microscope shows that a subpopulation
212 of D1R+ AStria neurons, located in a posterior - ventral hotspot of the tail striatum, responds to

213 footshocks. During the course of fear learning, these neurons increasingly code for an aversively-
214 motivated CS, and for freezing to movement transitions, in a highly inter-dependent fashion.
215
216 **Coding for footshocks and movement by Adora+ AStria neurons**
217 The other large population of principal neurons in the AStria are Adora+ neurons which, in analogy
218 to other striatal areas, represent neurons of an "indirect" pathway through the basal ganglia (Gerfen
219 et al., 1990; Gangarossa et al., 2019). We next investigated the *in-vivo* activity of this population of
220 AStria neurons throughout the three-day fear learning protocol, using an $Adora^{Cre}$ mouse line to
221 target the expression of GCamp6 to Adora+ neurons (Figure 3A-D; see Materials and Methods).
222 More than half of the Adora+ AStria neurons responded to footshocks on day 2 (148/251 neurons;
223 Figure 3C; 3E-F). A smaller subpopulation (~ 10%) responded to individual tone beeps during the
224 CS (see Figure 3G for an example neuron). However, different from the D1R+ neurons, the
225 percentage of tone (CS) - responsive neurons did not change during fear learning, and the
226 population response to tones was modest throughout the three days of fear learning (Figure 3 H,
227 Chi^2 test for trend, $p = 0.698$) (see also Figure 3I; Figure 3, Figure Suppl. 1). The response fidelity
228 was found to be different between days (Figure 3J, KW test, $p = 0.011$), with a slight decrease from
229 the training - to the retrieval day (Figure 3J, Dunn's MC test, $p = 0.012$), whereas the estimated AP
230 content of the Ca^{2+} events showed no change across the fear learning days (Figure 3K, KW test, $p =$
231 0.457). Thus, a subpopulation of Adora+ neurons in the AStria responds to footshocks, but the
232 number of Adora+ neurons that responds to tones (CS) is relatively small, and remains largely
233 unchanged during fear learning.
234
235 We next analyzed whether the activity of Adora+ AStria neurons was modulated by the movement-
236 or freezing state of the mice. We first restricted the analysis to the 30-s intervals of CS stimuli, and
237 found for these times that a sub-population of Adora+ neurons responded to movement onset
238 (Figure 3L). ROC showed that the number of Adora+ neurons with a movement response increased

239 during day 2 and day 3 of the fear learning protocol (Figure 3M, $p = 0.0016$, Chi^2 test for trend).
240 The increase in movement-ON responses was also visible in PSTHs over the entire population of
241 imaged Adora+ neurons (Figure 3N). The response fidelity of movement-ON responses was
242 significantly different between the three days of the fear learning protocol, with a significant
243 increase between day 1 and day 2, and between day 2 and 3 (Figure 3O, $p < 0.0001$, KW test
244 followed by Dunn's MC test; Hab_RF vs. Train_RF, $p < 0.0001$; Hab_RF vs. Ret_RF, $p < 0.0001$),
245 while the estimated AP content was unchanged (Figure 3P, $p = 0.281$, KW test). Corresponding to
246 an increased activity at movement onset, aligning the activity of Adora+ AStria neurons to the
247 onset of freezing revealed a decreased activity (Figure 3, Figure Suppl. 2). Finally, an analysis of
248 the movement-ON responses of Adora+ neurons in the absence of a CS revealed only a small
249 response (Figure 3Q). Taken together, these experiments reveal that during the course of fear
250 learning, an increasing percentage of Adora+ AStria neurons coded for movement onset.
251
252 We next analyzed whether vice-versa, the responses to tones might be modulated by the movement
253 state of the mice. Indeed, the response fidelity of Adora+ neurons to tone beep stimulation was
254 significantly higher when the mice moved, as compared to when the mice froze, for all three days
255 of the fear learning protocol (Figure 3R, $p < 0.0001$ KW test followed by Dunn's MC test; Hab_Frz
256 vs. Hab_Mov, $p < 0.0001$; Train_Frz vs. Train_Mov, $p < 0.0001$; Ret_Frz vs. Ret_Mov, $p =$
257 0.0003). On the other hand, the estimated AP content of Ca^{2+} events evoked by tone stimulation
258 was not modulated by the movement state of the mice (Figure 3R; $p = 0.545$, KW test). These data
259 thus show, similar to D1R+ AStria neurons, that the transient movement-ON activity of Adora+
260 neurons is potentiated in the presence of a CS, and, vice-versa, that tone-driven activity is
261 potentiated by the movement of the mouse.
262
263 In order to assess the interaction between movement-state dependent activity, and CS-driven
264 activity in $Adora^+$ AStria neurons more comprehensively, we next analyzed their average Ca^{2+}

event frequencies for the four combinations of movement states / tone representations, separately for each day of the fear memory protocol (Figure 3S). A KW test showed that the Ca^{2+} event frequencies differed across categories (Figure 3S; $p < 0.0001$). Given that the mice moved, the activity of Adora+ neurons was unchanged by a CS (Dunn's MC test, Mov_noCS_Hab vs. Mov_CS_Hab, $p = 0.99$); as in the data for the D1R+ neurons, the paucity of freezing events on the habituation day did not allow us to make statistical comparisons with data obtained in the freezing state on day 1. During the training day, the average Ca^{2+} event frequencies were ~ 2-fold lower during the freezing state as compared to the movement state, both in the presence- and in the absence of the CS (Figure 3S, Dunn's MC test, Frz_noCS_Train vs. Mov_noCS_Train, $p < 0.0001$; Frz_CS_Train vs. Mov_CS_Train, $p < 0.0001$). On the other hand, for a given movement or freezing state, the presence or absence of the CS did not significantly change the activity of Adora+ neurons, and the same was true for the retrieval day (Dunn's MC test, $p > 0.05$ for all comparisons, see statistics Table for Figure 3 for exact p values). Furthermore, on the retrieval day, the activity of Adora+ neurons was again higher in the movement - than in the freezing state, both in the absence and presence of the CS (Figure 3S, Dunn's MC test, Frz_noCS_Ret vs. Mov_noCS_Ret, $p < 0.0001$; Frz_CS_Ret vs. Mov_CS_Ret, $p < 0.0001$). This analysis revealed that overall, the neuronal representation of movement in Adora+ AStria neurons is less influenced by fear learning than in the D1R+ neurons (Figure 1); the learning - induced activity change might consist in a downregulation of the activity of Adora+ neurons in the freezing state. Another difference to the D1R+ neurons is the finding that the CS did not have a primary importance for the activity of Adora+ neurons (Figure 3S).

Taken together, a large population of $Adora^{+}$ AStria neurons shows robust responses to footshocks. Only a small fraction of these neurons, however, responds to the CS and these responses are not modulated by fear learning (Figure 3H-K). Adora+ neurons, on the other hand, show a transient response to movement onset given that a CS is present, and fear learning increases the number of

291 Adora^{+} neurons with such a response. The spatial distribution of footshock- and movement-ON
292 responding Adora+ neurons was broader, and the responding neurons were located more anteriorly
293 as compared to the responding D1R+ neurons (Figure 3T, U; compare to Figure 2A-C). Finally, we
294 found that the percentage of active Adora^{+} neurons on the training day was high (~ 75%; Figure
295 3V), primarily because a large percentage of the Adora+ neurons is activated by footshocks.
296 However, only a relatively small population of Adora+ AStria neurons maintained their activity in
297 response to the CS and to movement-ON events on the fear memory retrieval day (Figure 3V).
298 Thus, *in-vivo* Ca^{2+} imaging reveals similarities, as well as differences in the response types and in
299 the plasticity of responses during fear learning between D1R+ and Adora+ neurons in the AStria.
300

301 **D1R+ and Adora+ AStria neurons do not instruct freezing or movement**

302 Our *in-vivo* Ca^{2+} imaging experiments showed that the two main populations of AStria principal
303 neurons code for footshocks, for the CS (in the case of the D1R+ neurons) and for movements, and
304 that many of these representations were changed during the course of fear learning (Figure 1-3).
305 We next wished to investigate whether, and how D1R+ and Adora+ AStria neurons might
306 contribute to fear learning. A classical model of basal ganglia function postulate that D1R+ neurons
307 in the direct pathway initiate movement, whereas Adora+ (or D2R+) neurons in the indirect
308 pathway suppress movements (Kravitz et al., 2010; Nelson and Kreitzer, 2014; but see Klaus et al.,
309 2019). Thus, one possible straightforward hypothesis is that activity of Adora+ neurons of the
310 AStria instructs an arrest of movement, or freezing, and vice-versa, that D1R+ neurons might
311 instruct movement re-initiation. We wished to test this hypothesis by optogenetic activation of
312 either D1R+ - or Adora+ AStria neurons, at times when the mice are engaged in regular exploratory
313 behavior. For this, we used the channelrhodopsin variant Chronos, which we expressed bi-laterally,
314 and Cre-dependently in D1R+, or Adora+ neurons of the AStria, using
315 AAV1:hSyn:FLEX:Chronos-eGFP in the respective Cre-mouse line (Figure 4A). Three to four
316 weeks later, the mice were allowed to explore the fear conditioning chamber, and trains of

317 optogenetic stimuli were applied (50 light pulses of 1 ms length at 25 Hz, repeated six times for
318 each mouse). Optogenetic stimulation did not lead to changes in the movement activity of the
319 $D1R^{Cre}$ mice, nor of the $Adora^{Cre}$ mice (Figure 4B, C; N = 8 and 8 mice, respectively; p = 0.621 and
320 0.163 respectively, paired t-test). These experiments suggest that in naive mice, the activity of
321 $Adora^{+}$ neurons is not sufficient to instruct freezing. Similarly, the activity of D1R+ AStria neurons
322 was not sufficient to modulate the movement activity of the mice, although we cannot exclude that
323 a role of the D1R+ neurons was masked by ongoing movement.
324
325 **Plasticity of the D1R+ AStria network contributes to fear learning**
326 We found above that many D1R+ AStria neurons respond to footshocks, and that following fear
327 learning, a partially overlapping population of $D1R^{+}$ neurons becomes activated during the CS,
328 given that the animal moved at the same time (Figures 1, 2). This suggests that fear learning drives
329 plasticity in D1R+ AStria neurons. To investigate the role of this aversively-motived plasticity in
330 fear learning, we next silenced the activity D1R+ AStria neurons during footshock presentation,
331 and observed the effects of this manipulation on freezing behavior during the training day, and one
332 day later during fear memory retrieval. The rationale behind this manipulation is that a strong
333 activity of D1R+ AStria neurons during the footshock (Figure 1) is likely a major drive for
334 plasticity at input synapses onto these neurons, and that blocking the footshock-evoked activity
335 likely also blocks plasticity.
336
337 For optogenetic silencing, we expressed the light-sensitive proton pump Archaerhodopsin (Arch;
338 Chow et al., 2010) in a Cre-dependent manner bilaterally in the AStria of $D1R^{Cre}$ mice, and
339 implanted optic fibers over each AStria (Figure 5A, B). Mice in a control group were injected with
340 an AAV vector driving the expression of eGFP (Materials and Methods). Four weeks later, both
341 groups of mice underwent auditory-cued fear learning, and on the training day yellow laser light
342 (561 nm) was applied for 3s, starting 1s before each footshock, with the aim to suppress footshock-

evoked activity in Arch-expressing D1R+ neurons (Figure 5C, D). We found in *ex-vivo* experiments that yellow light strongly hyperpolarizes Arch-expressing D1R+ and Adora+ AStria neurons, suppresses action potential (AP) firing, and does not evoke rebound APs when the light is switched off (Figure 5, Figure Suppl. 1).

During the habituation day of the fear learning protocol the mice showed little freezing, as expected (Figure 5E). On the training day, during which mice received a 1s footshock after each tone block, mice in both groups showed increasing levels of freezing throughout the training period (Figure 5F; CS periods and footshocks are indicated by blue and yellow vertical lines). Freezing levels were not different between the Arch- and the control group, neither for the CS- nor for the no-CS epochs (Figure 5G, left, for the CS epochs; $p = 0.386$; Figure 5G right, for the no-CS epochs; $p = 0.249$; 2-way RM-ANOVA). Thus, optogenetic silencing of the footshock-evoked activity of D1R+ AStria neurons did not change the freezing behavior of mice during the training day.

On the third day, we tested for fear memory retrieval by applying tone stimulation (CS) alone in a different context (see Materials and Methods). The time-resolved freezing analysis revealed a gradual increase of freezing levels when mice entered the conditioning chamber (to ~ 20%; Figure 5H, arrow). This baseline level of freezing has been observed before (Cummings and Clem, 2020), and likely represents a residual contextual fear memory, despite the change of the context between the training day and the retrieval day (see Materials and Methods). The 30-s CS blocks caused a vigorous increase in freezing in eGFP-expressing control mice, whereas in the Arch - expressing mice, the CS was less efficient in driving freezing (Fig. 5H, black- and green average traces, N = 9 eGFP- and N = 11 Arch -expressing $D1R^{Cre}$ mice). Averaging and statistical analysis revealed a significant difference in CS-driven freezing between control - and Arch -expressing $D1R^{Cre}$ mice (Figure 5I, closed data points; $p = 0.023$, two-way RM- ANOVA). On the other hand, freezing during the no - CS epochs was unchanged between the two groups (Figure 5I, open data points; p =

369 0.541, 2-way RM-ANOVA). Thus, optogenetic inhibition of D1R+ AStria neurons during the
370 aversive footshocks on the training day causes a diminished auditory-cued recall of fear memory
371 one day later. This suggests that D1R+ AStria neurons contribute to auditory-cued fear learning.
372
373 **The Adora+ AStria network suppresses learned contextual fear**
374 We next investigated the role of footshock-driven activity in the Adora$^+$ AStria network for
375 auditory-cued fear learning. For this, we silenced the activity of Adora$^+$ AStria neurons during the
376 footshocks on the fear memory training day (Figure 6A-C), in an approach analogous to the one
377 used above for the D1R$^+$ neurons. During the habituation day, we observed low freezing as
378 expected (Figure 6D). On the training day, mice in both the eGFP - expressing control group and in
379 the Arch group showed a gradual increase in freezing with successive CS - US pairings, interrupted
380 by low freezing activity immediately following the footshocks, caused by running and escape
381 behavior (Figure 6E). The analysis of freezing during the CS - and no-CS epochs revealed no
382 difference in the freezing levels between the Arch - and the eGFP groups (Figure 6F; $p = 0.375$ and
383 $p = 0.196$ respectively; 2-way RM ANOVA). Thus, similar as for the D1R$^+$ neurons, footshock-
384 driven activity in Adora$^+$ AStria neurons is not necessary for freezing behavior that develops during
385 the training day.
386
387 On the fear memory recall day, the dynamics of the fear behavior differed between the eGFP and
388 the Arch group (Fig. 6G, H). While the eGFP - expressing control mice displayed an increased
389 freezing during each CS epoch followed by a relaxation to lower freezing levels, mice in the Arch
390 group showed a delayed relaxation of freezing following the CS epochs (Figure 6G; black and red
391 traces respectively). To quantify these effects, we analyzed the average time spent freezing during
392 the CS and during a late no-CS epoch (Figure 6G, blue vertical bar, and grey stripes). This showed
393 that freezing during the no-CS epochs was *increased* in the Arch group as compared to eGFP
394 controls (Figure 6H, right; $p = 0.041$; 2-way RM ANOVA), whereas freezing during the CS epochs

395 was unchanged between the Arch - and the control group (Figure 6H, left; p = 0.548; 2-way RM-
396 ANOVA). Thus, surprisingly, footshock - driven plasticity of Adora+ AStria neurons causes a
397 suppression of learned freezing in the *absence* of the auditory cue during fear memory retrieval.
398 This finding, together with the results obtained from silencing $D1R^+$ AStria neurons (see above),
399 establishes separate, but functionally synergistic roles of the direct- and indirect pathway neurons
400 of the AStria in fear learning. In fact, the action of both sub-systems together increases the
401 difference between the strength of a defensive behavior in the presence, and absence of a learned
402 aversive sensory cue.
403
404 **Brain-wide screening of presynaptic inputs to the AStria**
405 Our *in-vivo* Ca^{2+} imaging and optogenetic experiments have revealed a differential role of D1R+ -
406 and Adora+ AStria neurons in auditory-cued fear learning. To start investigating the role of
407 synaptic afferents to AStria neurons in these plasticity processes, we next used monosynaptic
408 retrograde rabies virus tracing to identify the presynaptic neuron pools that provide input to $D1R^+$
409 and $Adora^+$ neurons in the AStria (Fig. 7A; Wickersham et al., 2007; Wall et al., 2013); see
410 Materials and Methods).
411
412 Mice were injected into the AStria of either $D1R^{Cre}$, or $Adora^{Cre}$ mice with a mix of AAV-helper
413 viruses to render subsets of Cre-expressing neurons competent for EnvA-pseudotyped rabies virus
414 uptake, and to drive eGFP expression (Wickersham et al., 2007); see Materials and Methods for the
415 specific viruses). Three weeks later, a pseudotyped delta-G rabies vector driving the expression of
416 dsRed was injected at the same coordinates. In this way, starter cells at the injection site in the
417 AStria could be identified by GFP- and dsRed co-labelling (red) (Fig. 7B, cells appearing yellow in
418 the overlay); retrogradely-labelled neurons were identified based on their single dsRed expression.
419 The analysis of trans-synaptically labelled neurons was restricted to dsRed positive neurons outside
420 of the striatum. We placed all presynaptic neurons found in N = 2 $D1R^{Cre}$ and N = 2 $Adora^{Cre}$ mice

421 into brain-wide models, with cells from the two mice arbitrarily positioned on different brain sides
422 (Figure 7E, F; red and blue dots, respectively), and analyzed the number and density of back-
423 labelled neurons in each brain area. In both $D1R^{Cre}$ and $Adora^{Cre}$ mice, we found the highest
424 number and density of dsRed-expressing cells in the dorsal (granular and dysgranular) part of the
425 posterior insular cortex (pInsCx), and in the adjacent ventral part of the secondary somatosensory
426 cortex (S2; see also Figure 7 Table Suppl. 1 for a list of all brain structures with detected
427 presynaptic neurons)(Figure 7C, D, G, H). A sizeable number of back-labelled neurons was also
428 found in various areas of the primary somatosensory cortex (S1), in the globus pallidus externa
429 (GPe), and in the thalamic parafascicular nucleus (PF; Figure 7C, D, G, H; Figure 7, Figure Suppl.
430 1). The GPe and the PF stood out by having high densities of presynaptic neurons to both D1R- and
431 Adora-MSNs, even though their absolute numbers were not large (Figure 7G, H; black bars).
432 Although the brain-wide distribution of presynaptic input neurons to $D1R^{+}$ and $Adora^{+}$ AStria
433 neurons was overall similar, we detected differences on a finer scale (see Figure 7, Figure Suppl.
434 2). Because S2 and the pInsCx provided the largest number of input neurons to the AStria, we
435 analyzed the anterior - posterior localization of these neurons. This showed that presynaptic
436 neurons in the S2 and pInsCx that provide input to $D1R^{+}$ AStria neurons have the highest density at
437 bregma levels of ~ 0, whereas neurons in S2 and pInsCx that provide input to Adora+ AStria
438 neurons are located at somewhat more posterior positions (Figure 7I, J). Taken together, rabies-
439 virus mediated circuit tracing shows that the AStria receives its main cortical input from the S2 and
440 the pInsCx, followed by primary somatosensory areas. Thalamic areas like PF and VPM, and basal
441 ganglia like GPe, as well as limbic areas like CeA and BLA for the Adora+ neurons, also contain
442 sizeable numbers of neurons that provide input to the AStria.
443
444 **The posterior insular cortex provides strong excitatory drive to the AStria**
445 Retrograde rabies-virus labelling showed that the pInsCx, and the adjacent ventral S2 provide a
446 primary cortical input to the AStria (Figure 7). We next wished to functionally validate the putative

447 connection from the pInsCx to the AStria, using optogenetically-assisted circuit-mapping (Petreanu
448 et al., 2007; Little and Carter, 2013). For this, we injected a viral vector driving the expression of
449 Chronos (AAV8:hSyn:Chronos-eGFP; Klapoetke et al., 2014) into the pInsCx (Fig. 8A, B). We
450 used $D1R^{Cre}$ x tdTomato, or $Adora^{Cre}$ x tdTomato mice, to target patch clamp recordings to either of
451 the two principle neuron populations in the AStria four weeks later. Blue light pulses (1 ms) at
452 maximal light intensity evoked robust optogenetically-evoked EPSCs of 8.8 ± 1.6 nA in D1R+
453 AStria neurons (n = 12 cells), and of 2.5 ± 0.5 nA in Adora+ AStria neurons (n = 19; p = 0.002,
454 Mann Whitney test; Figure 8C-E). At both connections, gradually increasing the stimulus light
455 intensity led to a smooth increase of the EPSC amplitude, which shows that many axons from
456 pInsCx neurons converge onto each type of AStria neuron (Figure 8C, D). With high light
457 intensities, the optogenetically-evoked EPSC amplitudes saturated, suggesting that a maximal
458 number of input axons was activated (Figure 8C, D). The paired-pulse ratio (PPR) did not differ
459 between the two neuron types, whereas the excitation/inhibition (E/I) ratio was significantly
460 smaller in Adora+ AStria neurons as compared to D1R+ neurons (Figure 8, Figure Suppl. 1; PPR: p
461 = 0.208, unpaired t-test; E/I: p = 0.0054, Mann Whitney test). Taken together, optogenetically-
462 assisted circuit mapping shows that both D1R+ and Adora+ neurons of the AStria receive robust
463 excitatory inputs from neurons in the pInsCx. This, together with the monosynaptic rabies tracing
464 (Figure 7), identifies the pInsCx, together with the ventral S2, as main cortical input area to the
465 AStria.
466
467 **Fear learning causes opposite plasticity at synapses on D1R+ and Adora+ AStria neurons**
468 The *in-vivo* imaging data showed that many D1R+ and Adora+ AStria neurons robustly respond to
469 footshocks, and that during the course of fear learning, subpopulations of these neurons become
470 responsive to the CS and to movement-ON transitions (Figures 1-3). Furthermore, silencing each
471 AStria neuron population during the footshocks led to characteristic temporal changes in defensive
472 behavior during the fear memory retrieval day (Figures 5, 6). These findings suggest that plasticity

473 might take place at the synapses that drive D1R+ and Adora+ AStria neurons. We therefore tested
474 whether fear learning induces plasticity at the glutamatergic synapse from the pInsCx to the D1R+ -
475 and Adora+ AStria neurons. Measurements of the AMPA/NMDA ratio can be used as an assay for
476 postsynaptic forms of long-term plasticity following experience-dependent learning (Yin et al.,
477 2009; Shan et al., 2014; Rothwell et al., 2015). Similarly, changes in paired-pulse ratio can be used
478 to test whether presynaptic forms of long-term plasticity have occurred (Lucas et al., 2016). Thus,
479 we used optogenetically-assisted circuit mapping to ask whether fear learning induces signs of
480 plasticity at the synapses from the pInsCx to either D1R+ or Adora+ AStria neurons.
481
482 We injected $D1R^{Cre}$ x tdTomato mice, and in a separate series of experiments $Adora^{Cre}$ x tdTomato
483 mice, with an AAV vector to drive the expression of Chronos in neurons of the pInsCx. Three to
484 four weeks later, the mice were subjected to auditory-cued fear learning (Figure 8F). Following the
485 fear-memory retrieval session on day 3, which was performed to validate that mice had
486 successfully learned the CS, optogenetically-evoked EPSCs were recorded in slice preparations. A
487 control group of mice underwent the same protocols, but no footshocks were applied ("CS only"
488 group; Figure 8F). Optogenetically evoked EPSCs at the pInsCx to $D1R^{+}$ AStria connection
489 showed a significant increase of the AMPA/NMDA ratio in the CS + US group, as compared to the
490 CS-only group (Figure 8G; $p = 0.001$, unpaired t-test), suggesting that at this connection, a
491 postsynaptic form of LTP had occurred during fear learning. The paired-pulse ratio, however, was
492 unchanged (Figure 8G; $p = 0.974$, unpaired t-test; Figure 8, Figure Suppl. 2). Conversely, at the
493 pInsCx to Adora+ AStria connection, the AMPA/NMDA ratio was unchanged (Figure 8H, $p =$
494 0.162, unpaired t-test; see also Figure 8, Figure Suppl. 3), but interestingly, the paired-pulse ratio
495 was increased in the CS+US group as compared to the CS-only group (Figure 8H; $p = 0.001$, Mann
496 Whitney test). The latter finding suggests that fear learning might induce a presynaptic form of
497 LTD at the pInsCx to Adora+ AStria synapse. Thus, auditory-cued fear learning drives long-term
498 plasticity with opposite directions at cortical synapses onto $D1R^{+}$ and $Adora^{+}$ neurons in the AStria.

499 These differential forms of long-term plasticity might contribute to the complementary roles which
500 the two types of AStria neurons play during fear learning.
501
502
503 **Discussion**
504 We describe a role of a posterior striatal circuit, the amygdala-striatal transition zone (AStria) in the
505 formation of auditory-cued fear memories. *In-vivo* Ca^{2+}-imaging revealed that sub-populations of
506 D1R+ and Adora+ neurons in the AStria respond to tones, footshock stimulation, and the
507 movement state of the animal. During the course of fear learning both neuron populations
508 increasingly code for movement-ON transitions, and D1R+ neurons increased their responsiveness
509 to the CS, showing that neuronal coding in the AStria is changed in a plastic manner after fear
510 learning. *In-vivo* optogenetic silencing during the footshock presentations revealed a differential
511 role of each subsystem in fear learning. Whereas plasticity in the D1R+ neurons contributes to the
512 retrieval of a cue-dependent fear memory, the Adora+ network acts to suppress freezing in the
513 *absence* of a sensory cue. We used molecularly defined retrograde tracing approaches and *ex-vivo*
514 optogenetic circuit mapping to study the role of defined synaptic afferents onto each neuron class
515 of the AStria in fear learning. We found that neurons in the dorsal pInsCx, and in the adjacent
516 ventral S2 provide the main cortical input to AStria neurons. Measurements of optogenetically-
517 evoked EPSCs at the synapses arising from the pInsCx showed that fear learning induced opposite
518 forms of long-term plasticity at synapses onto D1R+ versus Adora+ AStria neurons. Taken
519 together, we find that direct and indirect pathway neurons in the AStria balance the amount of
520 learned fear behavior in the presence, and absence of relevant sensory cues.
521
522 **Plasticity of *in-vivo* responses of AStria neurons**
523 *In-vivo* Ca^{2+} imaging with a miniature microscope in freely moving mice showed commonalities
524 and differences in the *in-vivo* activity of D1R+ and Adora+ neurons of the AStria. In both neuron

525 types, footshocks evoked robust responses; the percentage of footshock-activated neurons was
526 higher in Adora+ than in D1R+ neurons. Following fear learning, the number of D1R+ neurons that
527 coded for the CS as well as for movement-ON transitions increased. Intriguingly, the responses to
528 the sensory stimulus (CS) and to the movement-state change potentiated each other, such that
529 following fear learning, D1R+ neurons responded best when the animals moved in the presence of
530 a CS (Figure 1T). Thus, the activity of D1R+ AStria neurons following fear learning might be seen
531 as a signal of heightened alertness, given that under natural conditions, the decision to move in the
532 presence of an aversive CS might expose the animal to harm. Movement - correlated activity has
533 been observed in striatal neurons (Markowitz et al., 2018), as well as in several types of sensory
534 cortices and also in a more brain-wide fashion (Niell and Stryker, 2010; Keller et al., 2012; Stringer
535 et al., 2019). Regarding the pInsCx, which as we show sends strong afferents to the AStria (Figure
536 7, 8), previous studies have shown somatosensory and auditory processing in this cortical area
537 (Rodgers et al., 2008; Sawatari et al., 2011; Gogolla et al., 2014), as well as state-dependent
538 signaling relating to physiological needs and to the aversive state of the animal (Livneh et al., 2017;
539 Gehrlach et al., 2019), although movement - ON responses have not been reported for the pInsCx.
540 Nevertheless, it is possible that the CS- and movement - state dependent activity of D1R+ neurons
541 is computed in an upstream cortical area like the pInsCx and/or the ventral S2. Alternatively,
542 movement-ON activity, and auditory (CS) information could be conveyed to D1R+ AStria neurons
543 from largely separate brain areas via different synaptic inputs, and summation of EPSPs would then
544 lead to a positive interdependence between both type of inputs. For example, based on previous
545 anatomical evidence and evidence from *in-vivo* stimulation experiments, it seems likely that the
546 auditory thalamus provides input to the AStria (Rogan and LeDoux, 1995; Polepalli et al., 2020).
547 Thus, the possibility that D1R+ AStria neurons extract information about the movement state and a
548 CS via distinct excitatory inputs which positively interfere with each other, could be investigated in
549 future studies.
550

551 The *in-vivo* activity of Adora+ AStria neurons and their changes after fear learning were different
552 in several respects from the one of D1R+ neurons. Fear learning did not induce a measurable
553 plasticity of the CS representation in Adora+ neurons (Figure 3). Furthermore, in Adora+ neurons
554 fear learning induced a difference in neuronal activity between the freezing - and the movement
555 state, but this difference was mainly caused by a *reduced* activity during the freezing state, apparent
556 both during the CS and in the absence of the CS (Figure 3S). This activity pattern was quite
557 different from the one of D1R+ neurons which showed an increased activity given that the animal
558 moved in the presence of a CS (see above). Thus, *in-vivo* Ca^{2+} imaging showed that population
559 coding of the CS and of movement states were differentially modulated by fear learning in the
560 direct-, and indirect pathway neurons of the AStria.
561
562 **Differential roles of direct- and indirect pathway AStria neurons in fear learning**
563 To investigate the role of the AStria in fear learning, we optogenetically inhibited D1R+ and
564 Adora+ AStria neurons during the presentation of footshocks on the training day. The rationale for
565 this manipulation was that significant populations of each neuron type robustly responded to
566 footshocks on the fear learning training day (Figures 1, 3). Therefore, silencing the footshock -
567 driven activity of these neurons should reduce an important driving force for aversively motivated
568 plasticity. This manipulation, applied to D1R+ neurons, led to a reduced amount of CS-driven
569 freezing during fear memory retrieval (Figure 5), showing that plasticity of D1R+ neurons
570 contributes to the formation of an auditory cued fear memory. Many aspects of plasticity in D1R+
571 AStria neurons, and their contribution to an auditory-cued fear memory, can be seen as analogous
572 to the role of LA principal neurons in fear learning. Thus, D1R+ neurons integrate US- and CS-
573 information (Figure 1), similar to LA neurons (LeDoux et al., 1990; Romanski et al., 1993).
574 Furthermore, D1R+ AStria neuron develop a sensitivity to the CS which is, in principle, similar to
575 the enhanced CS responses in the LA (Quirk et al., 1995; Amano et al., 2011; Grewe et al., 2017;
576 Zhang and Li, 2018), with the difference that the D1R+ AStria neuronal CS response is coupled to

577 the movement state of the animal, whereas movement -onset responses were not reported in the
578 above studies in the LA (note that more recent studies in the BA revealed additional coding for
579 behavioral states and behavioral decisions; (Kyriazi et al., 2018; Gründemann et al., 2019). Finally,
580 D1R+ AStria neurons show signs of postsynaptic LTP at a major cortical input after fear learning
581 (Figure 8); signs for postsynaptic LTP have been observed in LA- and/or BA neurons following
582 fear learning, when studying electrically stimulated thalamic - and cortical inputs (McKernan and
583 Shinnick-Gallagher, 1997; Tsvetkov et al., 2002; Rumpel et al., 2005; Namburi et al., 2015). Thus,
584 D1R+ AStria neurons contribute to the formation of an auditory - cue dependent fear memory, in
585 an analogous fashion as LA principal neurons. One difference between both systems are, however,
586 their different output structures: While LA neurons signal to the BA- and to the central amygdala
587 (see Duvarci and Paré, 2014 for a review), our preliminary evidence suggests that D1R+ AStria
588 neurons have a classical basal ganglia output to the Substantia nigra pars reticularis (Figure 8,
589 Figure Suppl. 4). Therefore, future work could investigate how D1R+ AStria neurons influence
590 downstream structures of the basal ganglia (Roseberry and Kreitzer, 2017), and how these are
591 ultimately merged with the amygdala - periaqueductal gray pathway (Tovote et al., 2016), to exert
592 an integrated control of fear behavior.
593
594 Intriguingly, optogenetic silencing experiments revealed a different role for the Adora+ AStria
595 neurons in fear learning. Silencing the Adora+ neurons during the footshock led to an *increased*
596 freezing, given that *no* CS was present during fear memory retrieval (Figure 6). This suggests that
597 following fear learning, footshock-driven plasticity of the Adora+ AStria neurons normally
598 *suppresses* freezing when no threat - predicting sensory cues are present. The differential role of
599 the D1R+ - and Adora+ AStria subsystems in fear memory is further apparent by the different types
600 of CS coding *in-vivo*, and by the different signs of long-term plasticity at the cortical input synapses
601 to each neuronal subsystem. We currently have only little direct evidence how the *in-vivo* activity
602 of Adora+ neurons in the AStria relates to defensive behavior. Nevertheless, our data is consistent

603 with the idea that a decreased activity after fear learning, given that the animal freezes (Figure 3S),
604 signals the absence of danger after the cessation of the learned CS, and might then "liberate" the
605 decision to move. Consistent with a model of a decreased activity of Adora+ neurons is the
606 observation that the pInsCx to Adora+ AStria synapse shows a presynaptic form of LTD after fear
607 learning (Figure 8). Interestingly, the finding that the AStria Adora+ subsystem signals the absence
608 of danger, and therefore safety, resembles previous work which has correlated the *in-vivo* activity
609 of AStria neurons with safety learning, albeit without distinguishing between direct- and indirect
610 pathway neurons (Rogan et al., 2005). Taken together, our study shows differential roles for the
611 direct and indirect pathway neurons in the AStria: D1R+ neurons signal danger given that the
612 animal moves during a CS, whereas Adora+ neurons signal safety in the absence of a learned CS.
613
614 Subtle, but functionally important differences in the brain areas that project to D1R+ versus Adora+
615 AStria neurons might determine their different *in-vivo* responses, and the different role each type of
616 AStria neuron plays during fear learning. In addition, the different responses might also be caused
617 by different effects of dopamine in D1R+ versus Adora+ neurons (Gerfen et al., 1990; Hjorth et al.,
618 2020). Interestingly, recent work has shown that a specific class of midbrain dopamine neurons
619 innervates the posterior tail striatum, and that these dopamine projections are activated by salient,
620 but not by rewarding stimuli (Menegas et al., 2015; Menegas et al., 2018). Although footshock
621 stimuli were not tested in these studies, it is possible that aversive stimuli would similarly cause the
622 release of dopamine in the AStria. Indeed, footshock-driven activity of VTA dopamine neurons that
623 project to the BA was recently shown to contribute to fear learning; furthermore, the same study
624 has obtained anatomical evidence for a projection of VTA DAT+ neurons to the AStria (Tang et
625 al., 2020). Therefore, dopamine signaling in the AStria might contribute to the differential plasticity
626 observed here for the two types of AStria neurons, and to their roles in auditory-cued fear learning.
627

Our optogenetic activation experiments, performed in the naive state of the mice, did not reveal significant effects on the movement - or freezing behavior of mice (Figure 4). Earlier work has shown that bilateral stimulation of D1R+ neurons in the dorsomedial striatum causes an increase in movement, whereas activation of D2R+ neurons increases freezing (Kravitz et al., 2010). On the other hand, optogenetic activation of neurons in a more posterior region of the dorsal striatum did not induce movement, but modulated the performance in an auditory learning task (Guo et al., 2018). Our findings in the likewise posteriorly located AStria agree with Guo et al. (2018), showing that neuronal activity in the AStria is not sufficient for driving movement or freezing directly. Rather, the activity of AStria neurons, after plasticity induced by fear learning, seems to play a role during the retrieval of associative, sensory-cue driven fear memories.

Conclusion

In summary, we show a role for the AStria in temporally balancing the expression of learned fear in the presence, and absence of aversive sensory cues, thus balancing cue-specific reaction with a more generalized fear response. Adaptive fear discrimination is critically important for animal survival, but is dys-regulated in anxiety disorders (Sangha et al., 2020). Indeed, it was found that during fear generalization, PTSD patients exhibited stronger responses in the striatum, amygdala and insular cortex amongst other areas (Morey et al., 2020). Because fear expression in the absence of aversive sensory cues is downregulated by Adora+ neurons in the AStria, it is an intriguing possibility to harness the differential pharmacology of direct- and indirect pathway neurons together with *in-vivo* manipulations of plasticity (Creed et al., 2015), in an attempt to mitigate the effects of fear generalization.

654 **Methods**

655 *Animals*

656 All experimental procedures with laboratory animals (Mus musculus) were performed under
657 authorizations for animal experimentation by the veterinary office of the Canton of Vaud,
658 Switzerland (authorizations VD3274 and VD3518). The following mouse lines were used: 1)
659 $D1R^{Cre}$ (B6.129-Tg(Drd1a-cre)EY217Gsat/Mmucd; see Gong et al., 2007; MMRRC: 030778-
660 UCD; 2) $Adora^{Cre}$ (B6.FVB(Cg)-Tg(Adora2a-cre)KG139Gsat/Mmucd; see Gerfen et al., 2013;
661 MMRRC: 036158-UCD; 3) Cre-dependent tdTomato reporter line/Ai14 (B6.Cg-
662 Gt(ROSA)26Sor<tm9(CAG-tdTomato)Hze>/J; JAX stock #007909; Madisen et al., 2010). All
663 animals used for experiments were male mice without prior contact to female conspecifics.
664 Animals were group-housed under a 12/12 h light/dark cycle with food and water ad libitum until
665 separated into single cages one day before surgery. For behavioral experiments (Figure 5, 6), mice
666 from 1-2 litters were randomly assigned to control - (GFP - expressing) or effect group (Arch-
667 expressing).

668

669 *Viral vectors and injection coordinates*

670 For *in-vivo* Ca^{2+}-imaging experiments (Figures 1 -3), we injected AAV1:hSyn:FLEX:GCaMP6m
671 (200nl; 6.8 $x10^{12}$ vg[vector genomes]/ml; cat. 290-1; viral vector facility University of Zürich,
672 Switzerland), into the left AStria of $D1R^{Cre}$ or $Adora^{Cre}$ mice, using the following coordinates:
673 medio-lateral (ML) 3.2 mm; anterior-posterior (AP) -0.8 to -1.0 mm; dorso-ventral (DV) -4.3 mm
674 (from bregma). For the optogenetic activation experiments (Figures 4), we injected
675 AAV1:hSyn:FLEX:Chronos-eGFP (200nl; $2.80x10^{12}$ vg/ml; University of North Carolina - UNC
676 vector core, Chapel Hill, NC, USA) bi-laterally into the AStria of $D1R^{Cre}$ or $Adora^{Cre}$ mice. For the
677 optogenetic inhibition experiments (Figures 5, 6), we injected AAV1:CAG:FLEX:Arch-eGFP
678 (200nl; $2.05x10^{12}$ vg/ml; UNC vector core) bi-laterally into the AStria of $D1R^{Cre}$ or $Adora^{Cre}$ mice.
679 In earlier experiments AAV1:CBA:FLEX:Arch-eGFP (200nl;$5.48x10^{12}$ vg/ml; AV-1-PV2432;

University of Pennsylvania vector core, Philadelphia, PA, USA) was used; both Arch constructs correspond to the initially described "Arch" (Chow et al., 2010). Mice in the control group received AAV1:CAG:FLEX:eGFP (200nl; 4.4 x10^{12} vg/ml; UNC vector core).

For the *ex-vivo* optogenetically-assisted circuit-mapping experiments (Figure 8), D1R^{Cre} x tdTomato mice, or Adora^{Cre} x tdTomato mice were injected unilaterally into the posterior insular cortex with AAV8:hSyn:Chronos-eGFP (200nl; 6.5x10^{12} vg/ml; UNC vector core), at the following stereotaxic coordinates: ML 4.2 mm; AP -0.55 mm, DV -3.8 mm (from bregma). In some experiments, D1R^{Cre}- or Adora^{Cre} mice were used, and an AAV8:CAG:FLEX:tdTomato (200nl; 6.5x1012 vg/ml; UNC vector core) was additionally injected into the AStria (coordinates as above), to visualize D1R^{Cre} - or Adora^{Cre} - positive neurons for subsequent patch-clamp recordings.

Surgery for virus injection, GRIN lens and optical fiber implantation

The surgery for stereotactic injection of all viral vectors and fiber implantation was performed using male mice of the indicated genotype, of 42-56 days of age. The procedures were similar as described in (Tang et al., 2020). In short, a mouse was anesthetized with isoflurane (induction with 3%, maintained at 1%) and the head was fixed in a Model 940 stereotactic injection frame (David Kopf Instruments, Tujunga, CA, USA) using non-rupture ear bars (Zygoma Ear cups, Kopf Instruments Model 921). Local anesthesia was applied subcutaneously using a mix (50 µl) of lidocaine (1mg/ml), bupivacaine (1.25mg/ml) and epinephrine (0.625 µg/ml). After the skull was exposed, small craniotomies were drilled above the indicated coordinates for injection and fiber insertion. For fiber implantation, an additional craniotomy was made close to Lambda to insert an anchoring micro screw. Virus suspension was injected using pulled glass pipettes and an oil hydraulic micromanipulator (MO-10, Narishige, Tokyo, Japan) with an injection speed of ~ 60 nl/min. For *in-vivo* Ca^{2+}-imaging (Figures 1 - 3) or optogenetic experiments (Figures 4 - 6), a GRIN lens (600 µm / 7.3 mm ProView™ integrated lenses; cat. 1050-004413; Inscopix Inc, Palo Alto,

706 CA, USA) or custom made optical fiber implants, respectively, were implanted 350 µm above the
707 virus injection site(s). Prior to GRIN lens implantation, a 25G medical injection needle was slowly
708 inserted and retracted to facilitate the later insertion of the blunt-ended lens. To reduce deformation
709 of brain tissue due to continuous vertical pressure, we lowered the GRIN lens with alternating
710 down (150 µm) and up (50 µm) movements until the last 200 µm before the final position. Optic
711 fiber implants for *in-vivo* optogenetic experiments were custom-made of a 200 µm core / 0.39 NA /
712 230 µm outer diameter optic fiber (FT200EMT; Thorlabs Inc, Newton, NJ, USA) inserted into 1.25
713 mm outer diameter ceramic ferrules (CFLC230; Thorlabs) as described in (Sparta et al., 2012).
714 GRIN lens or optical fiber implants were treated with a light-curing adhesive iBond Total Etch
715 (Kulzer GmbH, Hanau, Germany) and secured in place by blue-light curing dental cement (Tetric
716 EvoFlow, Ivoclar Vivadent, Schaan, Liechtenstein). The open end of the GRIN lens at the
717 integrated docking platform was sealed using a Kwik-Sil silicone compound (World Precision
718 Instruments, Sarasota, FL, USA). After stitching, the skin was covered with Bepanthen® Plus
719 cream (Bayer AG, Leverkusen, Germany), the drinking water was supplemented with 1 mg/ml
720 paracetamol and the animals were monitored for the following 6 days to ensure proper post-
721 surgical recovery.
722
723 *Behavior*
724 Auditory-cued fear learning was tested three to four weeks after the surgery. Mice were handled by
725 the experimenter and habituated to the procedure of attachment/detachment of the optical patch
726 cords (before optogenetic experiments), or a dummy mini-microscope (Inscopix Inc.) to the GRIN
727 lens platform (before Ca^{2+}-imaging experiments), for 10-15 min on five consecutive days. An
728 auditory-cued fear learning paradigm was performed in a conditioning chamber of a Video Fear
729 Conditioning Optogenetics Package for Mouse (MED-VFC-OPTO-M, Med Associates Inc.,
730 Fairfax, VT, USA) under control of VideoFreeze® software (Med Associates Inc). On day 1
731 (habituation), a mouse at a time was connected to the optic fiber patch cords, or a nVista3.0 mini-

732 microscope (Inscopix Inc.) was attached, and the animal was placed in the conditioning chamber.
733 The latter was a rectangular chamber with a metal grid floor, cleaned with 70% ethanol. Six tone
734 blocks (CS), each consisting of 30 tone beeps (7 kHz, 80 dB, 100 ms long, repeated at 1 Hz for 30
735 s), were applied 90 s apart. On day 2 (training), the mouse was placed in the same chamber and
736 presented with six CS blocks pseudo-randomly spaced 60-120 s apart, each followed by a 1s foot
737 shock US (0.6 mA, AC) delivered by a stimulator (ENV-414S, Med Associates Inc). On day 3
738 (retrieval), the mouse was placed in a conditioning chamber within a different context, consisting
739 of a curved wall and a smooth acrylic floor, cleaned with perfumed general-purpose soap. Four CS
740 blocks as on days 1 and 2 were applied for fear memory recall (see Figure 1, Figure Suppl. 1 for the
741 timing of CS - and US stimuli).
742
743 For optogenetic silencing experiments with Arch (Figures 5, 6), light was delivered during 3s
744 starting 1s before the footshock via 200 µm core / 0.22 NA optic fiber patch cords (Doric Lenses,
745 Canada) from a 561 nm diode-pumped solid state laser (MGL-FN-561-AOM, 100 mW, Changchun
746 New Industries Optoelectronics Technology, Changchun, China). The laser was equipped with an
747 AOM and an additional mechanical shutter (SHB05T; Thorlabs). For optogenetic activation
748 experiments with Chronos (Figure 4), 1-ms light pulses were delivered at 25 Hz, 2s duration from a
749 473 nm diode-pumped solid-state laser (MBL-FN-473-150mW, Changchun New Industries
750 Optoelectronics Technology). The intensity of each laser was adjusted before the experiment to
751 deliver 10 mW light power at the fiber tip.
752
753 The behaviour of animals was recorded at video rate (30 Hz) by the VideoFreeze® software (Med
754 Associates Inc). Based on the behavioural videos, a movement trace was generated using ezTrack
755 software (Pennington et al., 2019); see e.g. Figure 1F-H, red trace). The experimenter, and the
756 person analyzing the data were blinded to the assignment of each mouse to the control - or test
757 group. The movement index trace from ezTrack was used to compute a binary freezing trace using

758 custom procedures in IgorPro 7 (WaveMetrics Inc, Lake Oswego, OR, USA). The animal was
759 considered to be immobile (freezing state) if the movement index was below a threshold of 40
760 arbitrary units (without cable attachment) or 120 a.u. (with cable attachment), for a minimum
761 duration of 0.5 s. The binned trace of percent time spent freezing (10s bin size; see e.g. Figures 4G,
762 J; 5F, H; 6E, G) was calculated as a time-average of the freezing state from the binary trace, and
763 then averaged across mice in each group. If mice from any experimental group showed low
764 freezing, they were excluded from the analysis; we used a threshold of 20% time spent freezing
765 during the fifth and sixth CS-blocks on day 2 (7 out of 59 mice for the behavioral experiments were
766 excluded).
767
768 *Microendoscopic Ca^{2+}-imaging data acquisition and analysis*
769 We used the nVista 3.0 system (Inscopix Inc.) for imaging the activity of either $D1R^+$ or $Adora^+$
770 neurons in the AStria over the three-day fear conditioning paradigm. Fluorescent images were
771 acquired at 30 Hz sequentially from three focal planes, resulting in an effective sampling rate of 10
772 Hz per plane. The intensity of excitation LED in the nVista3.0 miniature microscope was set to 1 –
773 1.5 mW/mm^2, and the camera gain was adjusted to achieve pixel values within the dynamic range
774 of the CCD.
775
776 The initial processing of *in-vivo* Ca^{2+}-imaging data was done using the Inscopix Data Processing
777 Software (IDPS; Inscopix Inc). This included: 1) deinterleaving of the videos into the frames taken
778 at individual focal planes; 2) spatial filtering; 3) motion correction; 4) manual selection of ROIs; 5)
779 removal of duplicates (i.e. cells from the neighboring focal planes if their intensity traces strongly
780 correlated with correlation coefficient > 0.9); 6) export of the absolute fluorescence traces for each
781 ROI and of individual timestamps into .csv files. TTL pulses delivered from the behavioral setup
782 (Med Associates) were used to align the Ca^{2+}-traces to CS or US events. The data were then
783 analyzed using custom routines in IgorPro 7 (WaveMetrics) as follows. From the absolute intensity

traces for each i-th cell ($F_i(t)$), Z-score traces were calculated as $Z_i(t) = \frac{F_i(t)-\langle F_i(t)\rangle}{\sigma(F_i(t))}$, where $\langle F_i(t)\rangle$ and $\sigma(F_i(t))$ are the mean and the standard deviation of the fluorescence intensity, respectively, calculated from the whole trace. $Z_i(t)$ traces were denoised with a low-pass finite impulse response filter (101 coefficients; end of the pass and start of the reject bands, 2 and 4 Hz respectively). To quantitatively analyze cellular responses, filtered Z-score traces $\acute{Z}_i(t)$ were deconvolved using Fourier transform with a kernel function approximating a unitary fluorescence response to a single AP, similar to the approach used in (Yaksi and Friedrich, 2006). For the kernel, a function $z(t) = (1 - e^{-t/\tau_{rise}}) \cdot e^{-t/\tau_{decay}}$ was assumed with the time constants τ_{rise}=0.08s and τ_{decay}=0.5s, respectively, with the peak amplitude set to 2.0. Deconvolution yielded a trace proportional to the AP firing rate $R_i(t) = FFT^{-1}\left[FFT\left[\acute{Z}_i(t)\right]/FFT[z(t)]\right]/\Delta t$ measured in [a.u./s] where Δt = 0.1s, sampling interval. The $R_i(t)$ traces were smoothed with a 3-points boxcar filter, and the local peaks exceeding a given amplitude threshold (generally set to 2 a.u./s) were detected using a first-derivative method. The time location (limited to 100 ms by sampling rate) and the amplitude of the peaks thus defined discrete Ca^{2+} events $E_i(t_j)$, which corresponded to the start of the rising phase of the j-th fluorescent transient seen in $F_i(t)$ and $Z_i(t)$. The amplitudes of the events from deconvolution (referred to as estimated AP content, EAC [a.u./s]) were proportional to the amplitude of the Ca^{2+}-transients (e.g. see Figure 1 - Figure Supplement 1E). With this method, we did not aim to infer exact AP spiking rates of cells (for which we lack temporal resolution), rather we interpret each "event" as a burst of several APs starting at a given timepoint, with the frequency of APs in a burst being proportional to EAC value.

Based on the timing and amplitudes of discrete events $E_i(t_j)$, we performed a receiver operating characteristic (ROC) analysis for sorting the cells by their strength of responses to a given sensory input (CS or US), or to a movement state transition (e.g. freeze - movement, or movement - freeze). For this, we calculated an auROC value for each cell (Britten et al., 1992) by comparing the

809 distribution of cellular responses taken as a sum of $E_i(t_j)$ amplitudes during test and baseline time
810 windows of the same duration. Baseline was chosen during periods irrelevant for the cell activity.
811 For tone responders, the baseline window was (-200;0) ms and the test window (0;200) ms relative
812 to tone beep onset at t = 0. For move-on transitions, the baseline window was a 600 ms window
813 close to the middle of a freezing bout outside the CS epoch; the test window was a (-300;300) ms
814 window centered on movement onset during CS tone blocks. To estimate the significance of the
815 calculated auROC value for each cell for a given stimulus, we compared these values with auROC
816 values obtained by random shuffling (1000x) of the test and baseline time windows. A neuron was
817 considered negatively or positively discriminative, if its auROC was below or exceeded,
818 respectively, 5% or 95% quantile of the shuffled auROCs (Li et al., 2017). For convenience, we
819 converted auROC values into the response strength values defined as $RS = (2 \cdot auROC - 1)$ (Li et
820 al., 2017). The cells were sorted according to their activity based on their RS values, and were
821 classified into responding or non-responding groups by the 5% / 95% quantile thresholds as
822 described above (e.g. see separation by the dashed line in Figures 1J, 1M, 3L). To construct
823 PSTHs, the event amplitudes $\boldsymbol{E_i(t_j)}$ [a.u./s] were cumulatively counted in a given time bin and
824 multiplied with its duration (100 ms), resulting in [a.u.].
825
826 *Rabies tracing*
827 For rabies tracing experiments (Fig. 7) D1R^{Cre} or Adora^{Cre} mice were injected into the AStria (see
828 above for coordinates) with a mix of AAVs (AAV8:hSyn:FLEX:TVA-2a-oG and
829 AAV8:hSyn:FLEX:H2B-GFP-2a-oG; 250 nl; 1:1), to render cells competent for EnvA-
830 pseudotyped rabies virus uptake (Wickersham et al., 2007; Wall et al., 2013). In later experiments,
831 we used a tricistronic vector; AAV1:hSyn:FLEX:TVA-2a-eGFP-2a-oG (250 nl; 5.3 x10^{12} vg/ml;
832 cat. 243-1; viral vector facility University of Zürich) to transduce the starter population. Three
833 weeks later, the rabies vector EnvA:deltaG–RV-dsRed (250 nl; viral vector core Salk Institute for
834 Biological Studies, La Jolla, CA, USA) was injected at the same coordinates. The animals were

835 sacrificed 7 days later, and a histological analysis was performed on every second 40 µm thick
836 coronal section of the entire brain, from the level of the prefrontal cortex up to the end of the
837 cerebellum. The resulting images were analysed in a semi-automatic fashion, i.e. dsRed positive
838 neurons were marked manually, brain sections were registered to the Allen brain atlas and marked
839 neurons were automatically mapped onto the resulting brain regions using Matlab-based software
840 (SHARP-Track; (Shamash et al., 2018). The positioning of all long-range projecting cells was
841 analysed and plotted on a 3D brain model using the python-based Brainrender software (Claudi et
842 al., 2020).
843
844 *Electrophysiology*
845 For whole-cell patch-clamp electrophysiology in slices, mice expressing Chronos in the insular
846 cortex (see above) were deeply anesthetized with isoflurane. After decapitation, the brain was
847 quickly removed from the skull and placed in ice-cold slicing buffer containing (in mM): 110
848 NMDG (N-methyl-D-glutamine), 2.5 KCl, 1.2 NaH_2PO_4, 20 HEPES, 25 Glucose, 5 Na- ascorbate,
849 2 Thiourea, 3 sodium pyruvate, 10 $MgCl_2$, 0.5 $CaCl_2$, saturated with carbogen gas (O_2 95%/CO_2
850 5%), pH of 7.4 adjusted with HCl. Coronal slices (300 µm) containing the ventral tail striatum were
851 cut using a Leica VT1200S slicer (Leica Microsystems, Wetzlar, Germany). Slices were stored for
852 7 min at 34°C in the slicing buffer and thereafter placed in a chamber containing a storage solution
853 containing (in mM): 92 NaCl, 2.5 KCl, 30 $NaHCO_3$, 1.2 NaH_2PO_4, 20 HEPES, 25 glucose, 5
854 sodium ascorbate, 2 Thiourea, 3 Na-pyruvate, 2 $MgCl_2$ and 2 $CaCl_2$, pH 7.4 at room temperature,
855 saturated with carbogen (Ting et al., 2014). Whole-cell patch-clamp recordings were performed
856 with a standard extracellular solution containing (in mM): 125 NaCl, 2.5 KCl, 25 $NaHCO_3$, 1.2
857 NaH_2PO_4, 25 glucose, 0.4 Na-ascorbate, 3 Myo-Inositol, 2 Na-pyruvate, 1 $MgCl_2$ and 2 $CaCl_2$,
858 pH7.4, saturated with carbogen gas. The set-up was equipped with an EPC10/2 patch-clamp
859 amplifier (HEKA Elektronik GmbH, Reutlingen, Germany), and an upright microscope (BX51WI;
860 Olympus, Tokyo, Japan) with a 60x / 0.9 NA water-immersion objective (LUMPlanFl, Olympus).

861

862 Patch-clamp experiments including E/I-ratio and AMPA/NMDA-ratio measurements (Figure 8)
863 were performed using a Cs^+-based intracellular solution (in mM): 140 Cs^+-gluconate, 10 HEPES, 8
864 TEA-Cl, 5 Na-phosphocreatine, 4 Mg-ATP, 0.3 Na-GTP, 5 EGTA, pH 7.2 adjusted with CsOH.
865 AMPA/NMDA - ratio experiments were done in the presence of 5µM $GABA_A$ receptor antagonist
866 gabazine (SR-95531; Abcam, Cambridge, UK). Experiments to test the archaerhodopsin (Arch)
867 properties (Figure 5 - Figure Supplement 2) were performed using a K^+-based solution with (in
868 mM): 8 KCl, 145 K-gluconate, 10 HEPES, 3 Na-phosphocreatine, 4 Mg ATP, 0.3 Na-GTP, 5
869 EGTA, pH 7.2 adjusted with KOH. All electrophysiological experiments were conducted at near-
870 physiological temperature (34°C) using an inlet heater SHM-6, a heated recording chamber RC-
871 26GL/PM-1 and a thermostatic control unit TC-344B (all from Warner Instruments, Holliston, MA,
872 USA). All chemicals, unless indicated, were from Sigma-Aldrich (St. Louis, MO, USA).
873

874 For activation of the excitatory and inhibitory opsins in slice experiments, and for visualization of
875 fluorophores in brain slices, high-power LEDs (CREE XP-E2, 480 nm and 530 nm; Cree Inc.,
876 Durham, NC, USA) were custom-coupled into the epifluorescence port of the microscope.
877 Illumination was controlled by the EPC10 amplifier DAC board connected to the LED driver
878 (BLS-1000-2, Mightex Systems, Toronto, Canada). Irradiance was measured by a photodiode
879 (DET36A/M, Thorlabs) coupled into the illumination light path, whose readings were calibrated by
880 the light power measured under the 60x objective using a power-meter model 1918-R equipped
881 with a 818-UV detector (NewPort, Irvine, CA, USA). Electrophysiological recordings were
882 analyzed in IgorPro (WaveMetrics) using the NeuroMatic plug-in (Rothman and Silver, 2018).
883

884 *Histology*

885 For anatomical analysis of optic fiber - or GRIN lens positions, mice were transcardially perfused
886 with a 4% paraformaldehyde (PFA) solution. The brains were post-fixed in PFA overnight and then

887 transferred to 30% sucrose in phosphate - buffered solution for dehydration. Coronal brain sections
888 of 40 µm thickness were prepared using a HM450 sliding microtome (Thermo Fisher Scientific,
889 Waltham, MA, USA). Slices were mounted on Superfrost® Plus slides (Thermo Fisher Scientific)
890 and embedded in Fluoroshield mounting medium containing DAPI to stain cell nuclei (Sigma-
891 Aldrich). Slices were imaged with a Slide Scanner VS120-L100 (Olympus) with a 10x/0.4 NA
892 objective, or with an upright Leica SP8 confocal microscope. Brain atlas overlays are taken from
893 (Franklin and Paxinos, 2016). The majority of brain structure names and their abbreviations follows
894 (Franklin and Paxinos, 2016); their correspondence to the Allen brain atlas are given in Figure 7,
895 Table Suppl. 1.
896
897 *Statistical analysis*
898 Statistical analysis was performed in GraphPad Prism 9 (GraphPad, San Diego, CA, USA). Before
899 choosing the main statistical test, the distribution of the data was tested for normality using a
900 Shapiro-Wilk test. When normality was confirmed, we used a paired or unpaired version of the
901 two-tailed Student's t-tests for two-sample datasets, as indicated. For the comparison of relative
902 datasets, we used a one-sample t-test. When the data was not normally distributed, we used two-
903 tailed non-parametric tests: a Wilcoxon matched-pairs signed-rank test for paired comparisons, or
904 Mann-Whitney U test for unpaired comparisons of two-sample datasets, as indicated.
905
906 For datasets with more than two samples (*in-vivo* Ca^{2+} imaging data; Figures 1, 3), the data showed
907 skewed distributions which did not pass the normality test, therefore we used a non-parametric
908 version of a one-way ANOVA, a Kruskal-Wallis test (KW test). If the KW test detected significant
909 differences, it was followed by Dunn's post-hoc test for multiple comparisons (called Dunn's MC
910 test). For datasets influenced by two factors such as the optogenetic silencing/control group and the
911 time of the experiment (Figures 5, 6), we used a repeated-measures two-way ANOVA (RM-

ANOVA) separately for the training and fear retrieval days. If RM-ANOVA reported significance, it was followed by Šidák's post-hoc tests for the respective factor.

The change in number of neurons responding *in-vivo* to different events across training (Figures 1K, 1N, 3H, 3M) was statistically assessed using a Chi-square test for trend. For the optogenetic silencing experiments, we determined the sample size *a priori* using a G*Power software (Faul et al., 2007) for an RM-ANOVA test (two groups, 4 replicate measurements for the fear retrieval day) assuming an average change in freezing of 20% (from 60 to 40%) and a standard deviation of 15% (resulting in an effect size of 0.667), significance level α=0.05, power 1-β = 0.85, and the correlation between repeated measures of 0.5. The resulting total sample size was N = 16 (N = 8 mice per group), with a critical F_{crit}= 4.6. There was no sample size estimation made for other experiments.

Each specific statistical test is mentioned in the Results text, and the input data along with statistical test summary (such as p-values, values of test statistics, degrees of freedom, etc.) and the main descriptive statistics are given in the statistics Tables for each relevant figure. The data are expressed as mean ± SEM. Statistical significance, if applicable, is indicated in the Figures using asterisks as $p \leq 0.05$ (*), $p \leq 0.01$ (**) and $p \leq 0.001$ (***).

Data availability

The essential raw data leading to the conclusions of this paper will be made available at 10.5281/zenodo.4003654.

Acknowledgements

We would like to thank Shriya Palchaudhuri and Denys Osypenko for helpful discussions regarding the analysis of freezing behavior. Images were acquired at the bio-optical imaging platform of

EPFL (BiOP). This work was supported by an EMBO fellowship to M.K. (# ALTF 224-2015), and by grants from the Swiss National Science foundation (SNSF; grant number 31003A_176332 / 1) and from the National Competence Center for Research (NCCR) of the SNSF "Synapsy - The Synaptic Bases of Mental disease", project P28 (both to R.S.).

944 **References**

945

946 Amano, T., Duvarci, S., Popa, D., and Paré, D. (2011). The fear circuit revisited: contributions of
947 the basal amygdala nuclei to conditioned fear. The Journal of neuroscience : the official journal of
948 the Society for Neuroscience *31*, 15481-15489.

949 Britten, K.H., Shadlen, M.N., Newsome, W.T., and Movshon, J.A. (1992). The analysis of visual
950 motion: a comparison of neuronal and psychophysical performance. The Journal of neuroscience :
951 the official journal of the Society for Neuroscience *12*, 4745-4765.

952 Burguiere, E., Monteiro, P., Mallet, L., Feng, G., and Graybiel, A.M. (2015). Striatal circuits,
953 habits, and implications for obsessive-compulsive disorder. Current opinion in neurobiology *30*,
954 59-65.

955 Chow, B.Y., Han, X., Dobry, A.S., Qian, X., Chuong, A.S., Li, M., Henninger, M.A., Belfort,
956 G.M., Lin, Y., Monahan, P.E., and Boyden, E.S. (2010). High-performance genetically targetable
957 optical neural silencing by light-driven proton pumps. Nature *463*, 98-102.

958 Claudi, F., Tyson, L.A., and Branco, T. (2020). Brainrender. A python based software for
959 visualisation of neuroanatomical and morphological data. bioRxiv
960 *https://doi.org/10.1101/2020.02.23.961748*.

961 Cox, J., and Witten, I.B. (2019). Striatal circuits for reward learning and decision-making. Nature
962 reviews. Neuroscience *20*, 482-494.

963 Creed, M., Pascoli, V.J., and Lüscher, C. (2015). Addiction therapy. Refining deep brain
964 stimulation to emulate optogenetic treatment of synaptic pathology. Science *347*, 659-664.

965 Cummings, K.A., and Clem, R.L. (2020). Prefrontal somatostatin interneurons encode fear
966 memory. Nature neuroscience *23*, 61-74.

967 Dalmay, T., Abs, E., Poorthuis, R.B., Hartung, J., Pu, D.L., Onasch, S., Lozano, Y.R., Signoret-
968 Genest, J., Tovote, P., Gjorgjieva, J., and Letzkus, J.J. (2019). A critical role for neocortical
969 processing of threat memory. Neuron *104*, 1180-1194 e1187.

970 Davis, M. (1992). The role of the amygdala in fear and anxiety. Annual review of neuroscience *15*,
971 353-375.

972 Dunsmoor, J.E., Prince, S.E., Murty, V.P., Kragel, P.A., and LaBar, K.S. (2011). Neurobehavioral
973 mechanisms of human fear generalization. NeuroImage *55*, 1878-1888.

974 Duvarci, S., and Paré, D. (2014). Amygdala microcircuits controlling learned fear. Neuron *82*, 966-
975 980.

976 Faul, F., Erdfelder, E., Lang, A.G., and Buchner, A. (2007). G*Power 3: a flexible statistical power
977 analysis program for the social, behavioral, and biomedical sciences. Behav Res Methods *39*, 175-
978 191.

979 Fanselow, M.S. (1994). Neural organization of the defensive behavior system responsible for fear.
980 Psychonomic bulletin & review *1*, 429-438.

981 Fanselow, M.S. (2018). The Role of Learning in Threat Imminence and Defensive Behaviors. Curr
982 Opin Behav Sci *24*, 44-49.

983 Franklin, K.B.J., and Paxinos, G. (2016). The Mouse Brain in stereotaxic coordinates. Elsevier /
984 Academic Press *4th edition*.

985 Gangarossa, G., Castell, L., Castro, L., Tarot, P., Veyrunes, F., Vincent, P., Bertaso, F., and
986 Valjent, E. (2019). Contrasting patterns of ERK activation in the tail of the striatum in response to
987 aversive and rewarding signals. J Neurochem *151*, 204-226.

988 Gehrlach, D.A., Dolensek, N., Klein, A.S., Roy Chowdhury, R., Matthys, A., Junghänel, M.,
989 Gaitanos, T.N., Podgornik, A., Black, T.D., Reddy Vaka, N.*, et al.* (2019). Aversive state
990 processing in the posterior insular cortex. Nature neuroscience *22*, 1424-1437.

991 Gerfen, C.R., Engber, T.M., Mahan, L.C., Susel, Z., Chase, T.N., Monsma, F.J., Jr., and Sibley,
992 D.R. (1990). D1 and D2 dopamine receptor-regulated gene expression of striatonigral and
993 striatopallidal neurons. Science *250*, 1429-1432.

994 Gerfen, C.R., Paletzki, R., and Heintz, N. (2013). GENSAT BAC cre-recombinase driver lines to
995 study the functional organization of cerebral cortical and basal ganglia circuits. Neuron *80*, 1368-
996 1383.

997 Ghosh, K.K., Burns, L.D., Cocker, E.D., Nimmerjahn, A., Ziv, Y., Gamal, A.E., and Schnitzer,
998 M.J. (2011). Miniaturized integration of a fluorescence microscope. Nat Methods *8*, 871-878.

999 Gogolla, N., Takesian, A.E., Feng, G., Fagiolini, M., and Hensch, T.K. (2014). Sensory integration
1000 in mouse insular cortex reflects GABA circuit maturation. Neuron *83*, 894-905.

1001 Gong, S., Doughty, M., Harbaugh, C.R., Cummins, A., Hatten, M.E., Heintz, N., and Gerfen, C.R.
1002 (2007). Targeting Cre recombinase to specific neuron populations with bacterial artificial
1003 chromosome constructs. The Journal of neuroscience : the official journal of the Society for
1004 Neuroscience *27*, 9817-9823.

1005 Graybiel, A.M. (2005). The basal ganglia: learning new tricks and loving it. Current opinion in
1006 neurobiology *15*, 638-644.

1007 Grewe, B.F., Gründemann, J., Kitch, L.J., Lecoq, J.A., Parker, J.G., Marshall, J.D., Larkin, M.C.,
1008 Jercog, P.E., Grenier, F., Li, J.Z., *et al.* (2017). Neural ensemble dynamics underlying a long-term
1009 associative memory. Nature *543*, 670-675.

1010 Grillner, S., Hellgren, J., Menard, A., Saitoh, K., and Wikstrom, M.A. (2005). Mechanisms for
1011 selection of basic motor programs - roles for the striatum and pallidum. Trends in neurosciences *28*,
1012 364-370.

1013 Gründemann, J., Bitterman, Y., Lu, T., Krabbe, S., Grewe, B.F., Schnitzer, M.J., and Lüthi, A.
1014 (2019). Amygdala ensembles encode behavioral states. Science *364*.

1015 Guo, L., Walker, W.I., Ponvert, N.D., Penix, P.L., and Jaramillo, S. (2018). Stable representation of
1016 sounds in the posterior striatum during flexible auditory decisions. Nature communications *9*, 1534.

1017 Hikosaka, O., Takikawa, Y., and Kawagoe, R. (2000). Role of the basal ganglia in the control of
1018 purposive saccadic eye movements. Physiological reviews *80*, 953-978.

1019 Hintiryan, H., Foster, N.N., Bowman, I., Bay, M., Song, M.Y., Gou, L., Yamashita, S.,
1020 Bienkowski, M.S., Zingg, B., Zhu, M., *et al.* (2016). The mouse cortico-striatal projectome. Nature
1021 neuroscience *19*, 1100-1114.

1022 Hjorth, J.J.J., Kozlov, A., Carannante, I., Frost Nylen, J., Lindroos, R., Johansson, Y., Tokarska,
1023 A., Dorst, M.C., Suryanarayana, S.M., Silberberg, G., *et al.* (2020). The microcircuits of striatum in
1024 silico. Proceedings of the National Academy of Sciences of the United States of America *117*,
1025 9554-9565.

1026 Humphries, M.D., and Prescott, T.J. (2010). The ventral basal ganglia, a selection mechanism at the
1027 crossroads of space, strategy, and reward. Progress in neurobiology *90*, 385-417.

1028 Hunnicutt, B.J., Jongbloets, B.C., Birdsong, W.T., Gertz, K.J., Zhong, H., and Mao, T. (2016). A
1029 comprehensive excitatory input map of the striatum reveals novel functional organization. eLife *5*.

1030 Janak, P.H., and Tye, K.M. (2015). From circuits to behaviour in the amygdala. Nature *517*, 284-
1031 292.

1032 Keller, G.B., Bonhoeffer, T., and Hubener, M. (2012). Sensorimotor mismatch signals in primary
1033 visual cortex of the behaving mouse. Neuron *74*, 809-815.

1034 Klapoetke, N.C., Murata, Y., Kim, S.S., Pulver, S.R., Birdsey-Benson, A., Cho, Y.K., Morimoto,
1035 T.K., Chuong, A.S., Carpenter, E.J., Tian, Z., *et al.* (2014). Independent optical excitation of
1036 distinct neural populations. Nat Methods *11*, 338-346.

1037 Klaus, A., Alves da Silva, J., and Costa, R.M. (2019). What, if, and when to move: Basal ganglia
1038 circuits and self-paced action initiation. Annual review of neuroscience *42*, 459-483.

1039 Kravitz, A.V., Freeze, B.S., Parker, P.R., Kay, K., Thwin, M.T., Deisseroth, K., and Kreitzer, A.C.
1040 (2010). Regulation of parkinsonian motor behaviours by optogenetic control of basal ganglia
1041 circuitry. Nature *466*, 622-626.

1042 Kyriazi, P., Headley, D.B., and Pare, D. (2018). Multi-dimensional Coding by Basolateral
1043 Amygdala Neurons. Neuron *99*, 1315-1328 e1315.

1044 LeDoux, J.E. (2000). Emotion circuits in the brain. Annual review of neuroscience *23*, 155-184.

1045 LeDoux, J.E., Farb, C., and Ruggiero, D.A. (1990). Topographic organization of neurons in the
1046 acoustic thalamus that project to the amygdala. The Journal of neuroscience : the official journal of
1047 the Society for Neuroscience *10*, 1043-1054.

1048 LeDoux, J.E., Iwata, J., Cicchetti, P., and Reis, D.J. (1988). Different projections of the central
1049 amygdaloid nucleus mediate autonomic and behavioral correlates of conditioned fear. The Journal
1050 of neuroscience : the official journal of the Society for Neuroscience *8*, 2517-2529.

1051 Li, Y., Mathis, A., Grewe, B.F., Osterhout, J.A., Ahanonu, B., Schnitzer, M.J., Murthy, V.N., and
1052 Dulac, C. (2017). Neuronal Representation of Social Information in the Medial Amygdala of
1053 Awake Behaving Mice. Cell *171*, 1176-1190 e1117.

1054 Little, J.P., and Carter, A.G. (2013). Synaptic mechanisms underlying strong reciprocal
1055 connectivity between the medial prefrontal cortex and basolateral amygdala. The Journal of
1056 neuroscience : the official journal of the Society for Neuroscience *33*, 15333-15342.

1057 Livneh, Y., Ramesh, R.N., Burgess, C.R., Levandowski, K.M., Madara, J.C., Fenselau, H., Goldey,
1058 G.J., Diaz, V.E., Jikomes, N., Resch, J.M.*, et al.* (2017). Homeostatic circuits selectively gate food
1059 cue responses in insular cortex. Nature *546*, 611-616.

1060 Lucas, E.K., Jegarl, A.M., Morishita, H., and Clem, R.L. (2016). Multimodal and site-specific
1061 plasticity of amygdala parvalbumin interneurons after fear learning. Neuron *91*, 629-643.

1062 Madisen, L., Zwingman, T.A., Sunkin, S.M., Oh, S.W., Zariwala, H.A., Gu, H., Ng, L.L., Palmiter,
1063 R.D., Hawrylycz, M.J., Jones, A.R.*, et al.* (2010). A robust and high-throughput Cre reporting and
1064 characterization system for the whole mouse brain. Nature neuroscience *13*, 133-140.

1065 Markowitz, J.E., Gillis, W.F., Beron, C.C., Neufeld, S.Q., Robertson, K., Bhagat, N.D., Peterson,
1066 R.E., Peterson, E., Hyun, M., Linderman, S.W.*, et al.* (2018). The Striatum Organizes 3D Behavior
1067 via Moment-to-Moment Action Selection. Cell *174*, 44-58 e17.

1068 McKernan, M.G., and Shinnick-Gallagher, P. (1997). Fear conditioning induces a lasting
1069 potentiation of synaptic currents in vitro. Nature *390*, 607-611.

1070 Menegas, W., Akiti, K., Amo, R., Uchida, N., and Watabe-Uchida, M. (2018). Dopamine neurons
1071 projecting to the posterior striatum reinforce avoidance of threatening stimuli. Nature neuroscience
1072 *21*, 1421-1430.

1073 Menegas, W., Bergan, J.F., Ogawa, S.K., Isogai, Y., Umadevi Venkataraju, K., Osten, P., Uchida,
1074 N., and Watabe-Uchida, M. (2015). Dopamine neurons projecting to the posterior striatum form an
1075 anatomically distinct subclass. eLife *4*, e10032.

1076 Morey, R.A., Haswell, C.C., Stjepanovic, D., Mid-Atlantic, M.W., Dunsmoor, J.E., and LaBar,
1077 K.S. (2020). Neural correlates of conceptual-level fear generalization in posttraumatic stress
1078 disorder. Neuropsychopharmacology *45*, 1380-1389.

1079 Namburi, P., Beyeler, A., Yorozu, S., Calhoon, G.G., Halbert, S.A., Wichmann, R., Holden, S.S.,
1080 Mertens, K.L., Anahtar, M., Felix-Ortiz, A.C.*, et al.* (2015). A circuit mechanism for differentiating
1081 positive and negative associations. Nature *520*, 675-678.

1082 Nelson, A.B., and Kreitzer, A.C. (2014). Reassessing models of basal ganglia function and
1083 dysfunction. Annual review of neuroscience *37*, 117-135.

1084 Niell, C.M., and Stryker, M.P. (2010). Modulation of visual responses by behavioral state in mouse
1085 visual cortex. Neuron *65*, 472-479.

1086 Pennington, Z.T., Dong, Z., Feng, Y., Vetere, L.M., Page-Harley, L., Shuman, T., and Cai, D.J.
1087 (2019). ezTrack: An open-source video analysis pipeline for the investigation of animal behavior.
1088 Sci Rep *9*, 19979.

1089 Petreanu, L., Huber, D., Sobczyk, A., and Svoboda, K. (2007). Channelrhodopsin-2-assisted circuit
1090 mapping of long-range callosal projections. Nature neuroscience *10*, 663-668.

1091 Phelps, E.A., and LeDoux, J.E. (2005). Contributions of the amygdala to emotion processing: from
1092 animal models to human behavior. Neuron *48*, 175-187.

1093 Polepalli, J.S., Gooch, H., and Sah, P. (2020). Diversity of interneurons in the lateral and basal
1094 amygdala. NPJ Sci Learn *5*, 10.

1095 Quirk, G.J., Repa, C., and LeDoux, J.E. (1995). Fear conditioning enhances short-latency auditory
1096 responses of lateral amygdala neurons: parallel recordings in the freely behaving rat. Neuron *15*,
1097 1029-1039.

1098 Redgrave, P., Rodriguez, M., Smith, Y., Rodriguez-Oroz, M.C., Lehericy, S., Bergman, H., Agid,
1099 Y., DeLong, M.R., and Obeso, J.A. (2010). Goal-directed and habitual control in the basal ganglia:
1100 implications for Parkinson's disease. Nature reviews. Neuroscience *11*, 760-772.

1101 Rodgers, K.M., Benison, A.M., Klein, A., and Barth, D.S. (2008). Auditory, somatosensory, and
1102 multisensory insular cortex in the rat. Cerebral cortex *18*, 2941-2951.

1103 Rogan, M.T., and LeDoux, J.E. (1995). LTP is accompanied by commensurate enhancement of
1104 auditory-evoked responses in a fear conditioning circuit. Neuron *15*, 127-136.

1105 Rogan, M.T., Leon, K.S., Perez, D.L., and Kandel, E.R. (2005). Distinct neural signatures for
1106 safety and danger in the amygdala and striatum of the mouse. Neuron *46*, 309-320.

1107 Romanski, L.M., Clugnet, M.C., Bordi, F., and LeDoux, J.E. (1993). Somatosensory and auditory
1108 convergence in the lateral nucleus of the amygdala. Behavioral neuroscience *107*, 444-450.

1109 Roseberry, T., and Kreitzer, A. (2017). Neural circuitry for behavioural arrest. Philos Trans R Soc
1110 Lond B Biol Sci *372*.

1111 Rothman, J.S., and Silver, R.A. (2018). NeuroMatic: An integrated open-source software toolkit for
1112 acquisition, analysis and simulation of electrophysiological data. Frontiers in neuroinformatics *12*,
1113 14.

1114 Rothwell, P.E., Hayton, S.J., Sun, G.L., Fuccillo, M.V., Lim, B.K., and Malenka, R.C. (2015).
1115 Input- and output-specific regulation of serial order performance by corticostriatal circuits. Neuron
1116 *88*, 345-356.

1117 Rumpel, S., LeDoux, J., Zador, A., and Malinow, R. (2005). Postsynaptic receptor trafficking
1118 underlying a form of associative learning. Science *308*, 83-88.

1119 Sacco, T., and Sacchetti, B. (2010). Role of secondary sensory cortices in emotional memory
1120 storage and retrieval in rats. Science *329*, 649-656.

1121 Sangha, S., Diehl, M.M., Bergstrom, H.C., and Drew, M.R. (2020). Know safety, no fear.
1122 Neuroscience and biobehavioral reviews *108*, 218-230.

1123 Sawatari, H., Tanaka, Y., Takemoto, M., Nishimura, M., Hasegawa, K., Saitoh, K., and Song, W.J.
1124 (2011). Identification and characterization of an insular auditory field in mice. The European
1125 journal of neuroscience *34*, 1944-1952.

1126 Schiffmann, S.N., and Vanderhaeghen, J.J. (1993). Adenosine A2 receptors regulate the gene
1127 expression of striatopallidal and striatonigral neurons. The Journal of neuroscience : the official
1128 journal of the Society for Neuroscience *13*, 1080-1087.

1129 Shamash, P., Carandini, M., Harris, K., and Steinmetz, N. (2018). A tool for analyzing electrode
1130 tracks from slice histology. bioRxiv *http://dx.doi.org/10.1101/447995*.

1131 Shan, Q., Ge, M., Christie, M.J., and Balleine, B.W. (2014). The acquisition of goal-directed
1132 actions generates opposing plasticity in direct and indirect pathways in dorsomedial striatum. The
1133 Journal of neuroscience : the official journal of the Society for Neuroscience *34*, 9196-9201.

1134 Sparta, D.R., Stamatakis, A.M., Phillips, J.L., Hovelso, N., van Zessen, R., and Stuber, G.D.
1135 (2012). Construction of implantable optical fibers for long-term optogenetic manipulation of neural
1136 circuits. Nat Protoc *7*, 12-23.

1137 Stringer, C., Pachitariu, M., Steinmetz, N., Reddy, C.B., Carandini, M., and Harris, K.D. (2019).
1138 Spontaneous behaviors drive multidimensional, brainwide activity. Science *364*, 255.

1139 Tang, W., Kochubey, O., Kintscher, M., and Schneggenburger, R. (2020). A VTA to basal
1140 amygdala dopamine projection contributes to signal salient somatosensory events during fear
1141 learning. The Journal of neuroscience : the official journal of the Society for Neuroscience *40*,
1142 3969-3980.

1143 Ting, J.T., Daigle, T.L., Chen, Q., and Feng, G. (2014). Acute brain slice methods for adult and
1144 aging animals: application of targeted patch clamp analysis and optogenetics. Methods in molecular
1145 biology *1183*, 221-242.

1146 Tovote, P., Esposito, M.S., Botta, P., Chaudun, F., Fadok, J.P., Markovic, M., Wolff, S.B.,
1147 Ramakrishnan, C., Fenno, L., Deisseroth, K.*, et al.* (2016). Midbrain circuits for defensive
1148 behaviour. Nature *534*, 206-212.

1149 Tovote, P., Fadok, J.P., and Lüthi, A. (2015). Neuronal circuits for fear and anxiety. Nature
1150 reviews. Neuroscience *16*, 317-331.

1151 Tsvetkov, E., Carlezon, W.A., Benes, F.M., Kandel, E.R., and Bolshakov, V.Y. (2002). Fear
1152 conditioning occludes LTP-induced presynaptic enhancement of synaptic transmission in the
1153 cortical pathway to the lateral amygdala. Neuron *34*, 289-300.

1154 Wall, N.R., De La Parra, M., Callaway, E.M., and Kreitzer, A.C. (2013). Differential innervation of
1155 direct- and indirect-pathway striatal projection neurons. Neuron *79*, 347-360.

1156 Weinberger, N.M. (2007). Auditory associative memory and representational plasticity in the
1157 primary auditory cortex. Hearing research *229*, 54-68.

1158 Wickersham, I.R., Lyon, D.C., Barnard, R.J., Mori, T., Finke, S., Conzelmann, K.K., Young, J.A.,
1159 and Callaway, E.M. (2007). Monosynaptic restriction of transsynaptic tracing from single,
1160 genetically targeted neurons. Neuron *53*, 639-647.

1161 Yaksi, E., and Friedrich, R.W. (2006). Reconstruction of firing rate changes across neuronal
1162 populations by temporally deconvolved Ca^{2+} imaging. Nat Methods *3*, 377-383.

Yin, H.H., Mulcare, S.P., Hilario, M.R., Clouse, E., Holloway, T., Davis, M.I., Hansson, A.C., Lovinger, D.M., and Costa, R.M. (2009). Dynamic reorganization of striatal circuits during the acquisition and consolidation of a skill. Nature neuroscience *12*, 333-341.

Zanette, L.Y., White, A.F., Allen, M.C., and Clinchy, M. (2011). Perceived predation risk reduces the number of offspring songbirds produce per year. Science *334*, 1398-1401.

Zhang, X., and Li, B. (2018). Population coding of valence in the basolateral amygdala. Nature communications *9*, 5195.

1173 **Figure Legends**

1174 **Figure 1**. **Miniature Microscope Ca^{2+}-imaging of D1R+ neurons in the AStria reveals**
1175 **interdependent coding for tones and movement during fear learning.**

1176 **(A)** Outline of the 3-day fear conditioning protocol. On the training day, after the tone a 1s, 0.6 mA
1177 footshock was applied (see inset on the *right*). **(B)** Experimental scheme of the injection of an AAV
1178 vector and placement of the GRIN lens in the Astria of $D1R^{Cre}$ mice. **(C)** Posthoc fluorescence
1179 microscopy image from an injected $D1R^{Cre}$ mouse expressing GCaMP6m (green). The black region
1180 indicates the position of the GRIN lens. The putative imaging area is depicted with a red rectangle.
1181 Scalebar, 500 µm. **(D-F) Z**-scored Ca^{2+} traces for three example neurons (black traces); movement
1182 traces of the mouse (red traces); freezing-state trace of the mouse (blue); and the color-coded z-
1183 scored Ca^{2+} traces for all neurons in one example mouse (bottom). Data are from the second CS
1184 presentation of day 1 (D), the fourth CS-US presentation of day 2 (E), and the second CS
1185 presentation on day 3 (F). **(G)** Six consecutive footshock responses of an example neuron (black)
1186 and the average trace (red). **(H)** PSTH of the footshock responses of all neurons (n = 167) imaged
1187 on day 2 in all $D1R^{Cre}$ mice (N = 8). The fraction of ROC - identified responders is depicted by the
1188 horizontal dashed line (n = 57). **(I)** Ca^{2+}-traces of an example neuron in response to all 120 tone
1189 beeps applied on day 3 (grey and black lines), and the average response (red). **(J)** PSTHs of tone
1190 responses of all cells on the training days, sorted by response strength. A significant response as
1191 determined by ROC was found in the neurons above the horizontal dashed line. **(K)** Percentage of
1192 neurons with a significant response, as determined by ROC, to tone stimulation for each day. **(L)**
1193 The PSTH of the tone beep response, averaged over the entire population of imaged neurons for
1194 each day. Note the increased tone responsiveness especially on the fear memory retrieval day (red
1195 trace). Blue and green traces depict data from the habituation- and training days, respectively. **(M)**
1196 PSTHs of the movement-onset responses in a similar display as above for tone responses (J),
1197 analyzed for times within CS presentations. **(N)** Percentage of neurons with a significant response
1198 to movement onset after freezing. **(O)** The PSTH of the movement onset response, averaged over

1199 the entire population of imaged neurons for each day. Color code is as in (L). (**P, Q**) Response
1200 fidelities (P), and estimated AP content of the Ca^{2+} events (Q) (see Materials and Methods) in
1201 response to movement onset, for the entire population of imaged neurons on day 1, 2 and 3 (blue,
1202 green, and red data, respectively). (**R**) The population PSTH of the movement onset response for
1203 each day, now analyzed in the *absence* of the CS ("no CS"). Note the smaller responses as
1204 compared to the movement - onset response in the presence of the CS (O, same y-scale). (**S**)
1205 Response fidelities and estimated AP content of the Ca^{2+} events for the tone responses, analyzed
1206 both during the freezing state of the mouse ("freeze") and when mice moved ("move"). Note the
1207 significantly higher response fidelity on day 3, and the significantly higher estimated AP-content
1208 on day 2 when mice moved as compared to the freezing state (see Results for statistical
1209 significance). (**T**) The frequency of Ca^{2+} events was analyzed separately for each of the four
1210 combinations of CS/no CS, and movement/Freezing states of the mice, for habituation day ("Hab"),
1211 training day ("train"), and fear memory retrieval day ("Ret"). The presence of a CS is indicated by
1212 the blue bars. The p - values for statistical significance are reported in the Results text, and can
1213 additionally be found the statistic Table for Figure 3.
1214
1215
1216

Figure 2. Spatial localization of the imaged D1R+ AStria neurons, and overlap of neurons coding for sensory events and movement state.

(**A-C**) Maps with the position of all imaged D1R+ AStria neurons, plotted as horizontal projection. Shown are the footshock-responses (A), the tone (CS) responses as imaged on day3 (B), and the movement - onset responses imaged on day 3 (C). Neurons are color - coded based on their respective ROC classification (red, responders, blue, non-responders) and size - coded based on their response amplitudes. For a coarse orientation, outlines of the amygdalar nuclei (basolateral amygdala; "BLA" and central amygdala, "CeA") and cortex ("Ctx") are shown. (**D**) Venn diagrams showing the overlap of neuronal populations within the D1R+ AStria neurons that respond to tones (green), to movement - onset transitions (blue), and to footshock stimulation on day 2 (red). Note the increased number of neurons responding to tones and movement - onset during fear memory retrieval, and the overlap of these sub-populations (right panel).

1232 **Figure 3. Adora+ AStria neurons code for footshocks and movement onset, but CS coding is**
1233 **less relevant than in D1R+ AStria neurons.**
1234 **(A)** Experimental scheme of the injection of an AAV vector and placement of the GRIN lens in
1235 Adora^{Cre} mice. **(B-D)** Ca^{2+}-traces for three example neurons (black); movement trace (red);
1236 freezing - state trace of the mouse (blue); and the color-coded Ca^{2+} traces for all neurons in this
1237 example mouse. Data are from the second CS presentation of day 1 (D), the fourth CS-US
1238 presentation of day 2 (E), and the second CS presentation on day 3 (F). **(E)** Six footshock responses
1239 of an example neuron (black) and the average trace (red). **(F)** PSTH of the footshock responses of
1240 all neurons (n = 251) imaged on day 2 in the D1R^{Cre} mice (N = 8). **(G)** Ca^{2+}-traces of an example
1241 neuron in response to all 120 tone beeps applied on day 3 (grey and black lines), and the average
1242 response (red). (**H**). Percentage of neurons with a significant response to tone stimulation for each
1243 day. **(I)** The population PSTH to tone beep stimulation, for habituation day (blue), training day
1244 (green), and fear memory retrieval day (red). (**J, K**). Response fidelities (J), and estimated AP
1245 content of the Ca^{2+} events (K) in response to tone stimulation for all neurons on day 1, 2 and 3
1246 (blue, green, and red data, respectively). **(L)** PSTHs of the movement-onset responses of all imaged
1247 neurons, analyzed for times within CS presentations. **(M)** Percentage of neurons with a significant
1248 response to movement onset after freezing. **(N)** The population PSTH of the movement onset
1249 response in the presence of the CS. Colour code is as in (I). (**O, P**) Response fidelities (O), and
1250 estimated AP content of the Ca^{2+} events (P) in response to movement onset for days 1, 2 and 3
1251 (color code as in J, K). (**Q**) The population PSTH of the movement onset response in the absence of
1252 the CS. (**R**) Response fidelities and estimated AP content of the Ca^{2+} events for the tone responses,
1253 analyzed both during the freezing state of the mouse ("freeze") and when mice moved ("move").
1254 Note the significantly higher response fidelities on all three days when the mice moved, as
1255 compared to the freezing state (see Results for statistical significance). (**S**) The frequency of Ca^{2+}
1256 events, analyzed separately for the four combinations of CS/no CS, and movement/Freezing states
1257 of the mice, for habituation day ("Hab"), training day ("train"), and fear memory retrieval day

("Ret"). The presence of a CS is indicated by the blue bars. The p-values for the indicated statistical comparisons are reported in the Results text. (**T, U**) Maps with the position of all imaged Adora+ AStria neurons from N = 8 mice, plotted in the same way as in Figure 2A-C for the D1R+ neurons. Shown are the footshock-responses (T), and the movement responses imaged on day3 (U). (**V**) Venn diagrams showing the overlap of neuronal populations within the Adora+ AStria neurons that respond to tones (green), to movement - onset transitions (blue), and to footshock stimulation on day 2 (red).

1272 **Figure 4. Optogenetic stimulation of D1R+ and Adora+ AStria neurons has no direct effect**
1273 **on movement.**
1274 **(A)** Scheme showing the bilateral placement of optic fibers over each AStria, and the injection of
1275 an AAV vector driving the Cre-dependent expression of Chronos. **(B)** Adora^{Cre} mice were allowed
1276 to explore the fear conditioning chamber, and trains of blue light stimuli (50 pulses of 1 ms length,
1277 25 Hz, duration of 2s) were applied. The average movement indices for N = 8 mice are shown,
1278 either centered around the time of light stimulation (red trace), or taken from a control time when
1279 no light was applied ("ctrl TP"). (**C**) Analogous experiment to the one in (B), now performed for
1280 D1R^{Cre} mice (N= 7). Note that optogenetic stimulation of neither Adora+ neurons (B), nor of D1R+
1281 neurons led to notable changes in the movement of mice.
1282
1283
1284
1285
1286
1287
1288

1289 **Figure 5. Optogenetic inhibition of D1R+ AStria neurons during footshock reduces auditory-**
1290 **cued fear memory retrieval one day later.**
1291 **(A)** Scheme showing the bi-lateral injections in $D1R^{Cre}$ mice of an AAV vector driving the
1292 expression of either Arch or eGFP (for controls), and the placement of optic fibers over each
1293 AStria. **(B)** Image of a coronal brain section at the indicated Bregma levels, illustrating the fiber
1294 placement (black arrows at fiber tip) and Arch expression (green). **(C)** Behavioral paradigm
1295 outlining the 3-day fear-learning protocol. **(D)** Scheme of the tone - footshock pairing, ending with
1296 a 1 s footshock. The time of the 3s yellow light application is indicated (yellow bar; a 3s constant
1297 light pulse of 561 nm and 10 mW at the fiber tip). **(E)** Freezing levels during 30s CS presentations
1298 on the habituation day for the control mice (expressing eGFP; black circles), and for Arch -
1299 expressing mice (green circles). **(F)** Time - binned average percent freezing traces for control mice
1300 (black data) and Arch - expressing mice (green data; bin width is 10 s in both cases). Light blue
1301 boxes indicate the 30s CS presentation periods. Grey bars indicate epochs of "no CS" analysis.
1302 Vertical orange lines indicate the times of footshock presentation. **(G)** Quantification of freezing
1303 during the training day for the control mice and Arch - expressing mice (black and green data,
1304 respectively). Freezing was averaged during the 30s CS presentations (filled circles, *left*) and for
1305 the no CS epochs (open circles, *right*). **(H)** Time-resolved freezing during the cued retrieval on day
1306 3. Note the phasic increases in freezing caused by each CS presentation (blue) in control mice
1307 (black trace, average of N = 9 eGFP expressing mice), which were smaller in amplitude in Arch -
1308 expressing mice (N = 11, green trace). **(I)** Quantification of freezing during the 30s CS presentation
1309 (*left*) and during the no CS epochs (*right*). Note the significant reduction of freezing during the CS
1310 in the Arch group (see Results for statistical significance).
1311
1312

1313 **Figure 6**. **Optogenetic inhibition reveals a role of Adora+ AStria neurons in suppressing**
1314 **learned freezing in the absence of a learned CS.**
1315 **(A)** Scheme of the experimental approach. **(B)** Example of a post-hoc validation of Arch expression
1316 (green) and the fiber placement (red dashed line) in the AStria of an Adora^{Cre} mouse. **(C)** Scheme
1317 of the tone - footshock pairing on the training day (left), and of the time of yellow light application.
1318 **(D)** Freezing levels during CS presentations on the habituation day for controls mice (expressing
1319 eGFP; black data) and Arch - expressing mice (red filled circles). **(E)** Time-resolved freezing
1320 analysis for control mice (black trace, average of N = 8 mice) and Arch - expressing mice (red
1321 trace, N = 10), displayed for 10 s bins. Bars and boxes have the same meaning as in Figure 5F. **(F)**
1322 Quantification of freezing during the 30s CS presentations (left), and during the 30s "no CS"
1323 epochs (right), both for control mice (black) and Arch - expressing mice (red). **(G)** Time-resolved
1324 freezing during the fear memory retrieval day. Color codes are as in (E). **(H)** Average percent of
1325 time spent freezing, analyzed during the 30s CS presentations (left), and during the no CS epochs
1326 (right) of the fear memory retrieval day, for both groups of mice. Note the significantly enhanced
1327 freezing in the Arch group at times when no CS was present (right; for statistical significance see
1328 Results).
1329

1330 **Figure 7. Retrograde transsynaptic tracing of brain-wide inputs to both D1R+ and Adora+**
1331 **AStria neurons.**
1332 **(A)** Scheme of the experimental protocol for rabies-virus mediated transsynaptic tracing. **(B)** *Left*,
1333 Example confocal images of the injection site in a D1R^{Cre} mouse, *Right*, confocal images at a
1334 higher magnification taken from the boxed area of the left image. Green, red and blue channels are
1335 eGFP-labelled cells expressing the helper viruses (green), rabies-virus expressing cells (red) and
1336 DAPI labelling (blue, only shown in the overlay images). Scale bars, 200 µm (*left*) and 50 µm
1337 (*right*). **(C, D)** Example widefield epifluorescence images of rabies virus - labelled presynaptic
1338 neurons in coronal sections, from a D1R^{Cre} mouse (C) and an Adora^{Cre} mouse (D). The
1339 abbreviations of brain areas are shown in Figure 7, Suppl. Table 1. Scalebars, 250 µm. **(E, F)**
1340 Localizations of presynaptic neurons plotted in a 3D brain model, both for D1R^{Cre} (E) and Adora^{Cre}
1341 (F) mice. Each brain shows the results of two animals (blue and red dots) with one dataset being
1342 artificially mirrored on the other hemisphere for each genotype. For orientation, some brain areas
1343 are highlighted (S2 – green, InsCtx – yellow, PF – red, BLA – pink). **(G, H)** Quantification of
1344 labelled neurons for each brain area. Upwards and downward data signify cell density and absolute
1345 number of cells, quantified for N = 2 mice of each genotype. Data from single animals are plotted
1346 as filled grey circles and triangles **(I, J)** Distribution of presynaptic neurons along the anterior -
1347 posterior axis in the insular cortex (I), and in the secondary somatosensory cortex (J). The dashed
1348 line indicates the border between the anterior and posterior insular cortex according to (Franklin
1349 and Paxinos, 2016).
1350

1351 **Figure 8. pInsCx provides strong excitatory inputs onto D1R+ - and Adora+ AStria neurons**
1352 **which show differential plasticity after fear learning.**
1353 **(A)** Experimental scheme of injection of an AAV vector driving the expression of Chronos into the
1354 pInsCx, and subsequent slice electrophysiology in the AStria. **(B)** *Left*, example fluorescence
1355 images of the injection site in the cortex expressing Chonos-eGFP (scalebar, 500 µm); *middle,*
1356 overview brightfield image with the position of the patch pipette (black dotted lines) in the AStria;
1357 *right*, higher magnification images examples of a recorded example cell (brightfield, *top*; and
1358 tdTomato fluorescence, *bottom*). **(C, D)** *Left*, EPSCs recorded by stimulating with 1 ms light pulses
1359 of increasing intensities (blue, photodiode-recorded trace), and *right*, the resulting input-output
1360 curve of EPSC amplitude versus light intensity, with data from all recorded cells overlaid. The
1361 example cell shown on the left is highlighted in black in the right panel. Data is shown for D1R+
1362 AStria neurons (C, n = 12 recordings) and Adora+ AStria neurons (D, n = 19 recordings). **(E)**
1363 Quantification of the maximal amplitude of EPSCs (*left*), and of the EPSC delay (*right*) measured
1364 in D1R+ - and Adora+ AStria neurons (n = 12 and n = 19, respectively). **(F)** Timeline of the *ex-*
1365 *vivo* patch-clamp plasticity experiments. See Results for details. **(G)** Example traces for NMDA-
1366 EPSCs recorded at +50 mV (top traces), and for AMPA-EPSCs at -70 mV (bottom traces),
1367 recorded in D1R+ neurons in each experimental group (*left*). The *right* panel shows the
1368 quantification of AMPA/NMDA ratios and paired-pulse ratios (50 ms inter-stimulus interval)
1369 recorded in each group of $D1R^{Cre}$ mice ("CS only", n = 11 recordings; "CS+US", n = 12). **(H)**
1370 Example AMPA-EPSC traces for the measurement of paired-pulse ratio (50 ms inter-stimulus
1371 interval) recorded in Adora+ neurons in each experimental group, as indicated. *Right*,
1372 quantification of AMPA/NMDA ratios, and paired-pulse ratios recorded in each group of $Adora^{Cre}$
1373 mice ("CS only", n = 12 recordings; "CS+US", n = 12).
1374

1375 **Figure Legends for Figure Supplements**

1376 **Figure 1, Figure Suppl. 1.**

1377 Exact timing of tone blocks (CS) and footshocks on each day of the fear learning protocol. Each
1378 tone block (CS presentation) consisted of n = 30 tone beeps (7 kHz, 80 dB) of 100 ms length,
1379 repeated at 1 Hz. On the training day, each CS was terminated by a 1s footshock (0.6 mA). For
1380 further details of the fear learning protocol, see Materials and Methods.

1381

1382 **Figure 1, Figure Suppl. 2.**

1383 (**A**) PSTH of movement - onset responses of all imaged D1R+ AStria neurons, in the *absence* of a
1384 CS.

1385 (**B**) Corresponding PSTH of the movement - onset responses, averaged over the entire population
1386 of imaged neurons. Note the only small population response to movement onset in the absence of a
1387 CS (compared with Figure 1L, during the CS).

1388

1389 **Figure 1, Figure Suppl. 3.**

1390 (**A, B**) PSTHs of Ca^{2+} event frequency for individual D1R+ neurons (A), and the population PSTH
1391 (B), aligned to freezing onset, for events that had occurred *during* the CS. Note the decreased Ca^{2+}
1392 event frequency at the onset of freezing on the training day and on the fear memory retrieval day
1393 (B, green and red traces).

1394 (**C**) A plot of the averaged event frequency, normalized to pre-freezing baseline, revealed a
1395 statistically significant reduction in Ca^{2+} event frequency during day 2 and day 3 ($p < 0.001$ for
1396 both; one-sample t-test).

1397

1398 **Figure 1, Figure Suppl. 4.**

1399 (A, B) PSTHs of Ca^{2+} event frequency for individual neurons (A), and the population PSTH (B),
1400 aligned to freezing onset in the *absence* of the CS.

1401 **Figure 3, Figure Suppl. 1.**

1402 PSTH of Ca^{2+} event frequency for individual Adora+ neurons, aligned to tone onset, irrespective

1403 whether the mouse moved, or froze. See Figure 3I for the corresponding population PSTH.

1404

1405 **Figure 3, Figure Suppl. 2.**

1406 (**A, B**) PSTH of Ca^{2+} event frequency for individual Adora+ neurons (A), and the corresponding

1407 population PSTH (B), aligned to the onset of freezing, for events that had occurred during the CS.

1408 (**C**) A plot of the averaged event frequency, normalized to pre-freezing baseline, revealed a

1409 significant reduction in event frequency during the fear memory retrieval day ($p < 0.001$; one-

1410 sample t-test).

1411

1412

1413

1414

1415

1416 **Figure 5, Figure Suppl. 1.**

1417 Properties of light-activated archaerhodopsin, as measured in D1R+ - and Adora+ AStria neurons

1418 in slice electrophysiology at 34°C.

1419 **(A)** An Adora^{Cre} x Ai14 mouse was injected with AAV1:CAG:FLEX:Arch-eGFP AAV vector into

1420 the Astria, and *in-vitro* patch-clamp recordings of Arch - expressing neurons were performed 3-6

1421 weeks later. Example of light-induced currents evoked by 300 ms exposures with increasing light

1422 (530 nm) intensities in an Adora+ neuron expressing Arch. Maximal light intensity was 15

1423 mW/mm^2; the holding potential was -70 mV.

1424 **(B)** Quantification of the maximal plateau current measured at the end of the light pulse (grey

1425 dashed box in A) for D1R+ - (n = 7) and Adora+ AStria neurons (n = 13) expressing Arch.

1426 **(C)** Example traces recorded in current-clamp showing that light exposure (3 s) was sufficient to

1427 block APs generated by a 1s current injection (no light, black trace; with light, red trace). This

1428 observation was made in all neurons recorded under current-clamp.

1429 **(D-F)** Repeated light exposures (300 ms pulses at 1 Hz, 30 times) were applied to test for the

1430 efficiency of repeated hyperpolarizations, and for possible rebound APs after light offset.

1431 Hyperpolarization (E) and rebound potentials (F) were quantified for D1R+ (n = 6) and Adora+

1432 AStria neurons (n=13).

1433

1434

1435 **Figure 7, Figure Suppl. 1**.

1436 Additional example images for transsynaptically retrogradely labelled neurons after injection of an
1437 AAV helper virus, and a rabies virus, into the AStria of a D1R^{Cre} mouse (A) and into the AStria of
1438 an Adora^{Cre} mouse (B). The images on the left sides illustrate a weak density of labelled neurons in
1439 the amygdalar region (left images, CeA, BLA, and LA, see also Figure 7 G, H for the
1440 quantifications). The images on the right sides illustrate labeling in a confined region of the PF
1441 (right images), which led to a notably high *density* of back-labelled neurons in the PF (see also
1442 Figure 7 G, H for the quantifications, and Figure 7, Figure Suppl. 1 - Table for the abbreviations of
1443 brain areas).

1444

1445 **Figure 7, Figure Suppl. 2**.

1446 Analysis of the number of back-labelled neurons in Adora^{Cre} mice *relative* to D1R^{Cre} , according to
1447 the analysis of cell numbers shown in Figure 7G, H. The numbers were sorted according to
1448 relatively stronger back-labelling of brain areas observed in Adora^{Cre} mice than in D1R^{Cre}
1449 (beginning on the left hand side). Note that Adora+ AStria neurons showed larger proportions of
1450 back-labelled presynaptic neurons in the lateral amygdala (LA), basolateral amygdala (BLA),
1451 central amygdala (CeA), temporal association cortex (TeA), and auditory cortex (AUD), as
1452 compared to D1R+ neurons; interestingly, these areas represent limbic - auditory areas with roles in
1453 associative learning (LeDoux, 2000; Weinberger, 2007; Sacco and Sacchetti, 2010; Dalmay et al.,
1454 2019). On the other hand, a higher proportion of neurons providing input to D1R+, as compared to
1455 Adora+ AStria neurons, was found in the S1, in the somatosensory thalamus (VPM), motor cortex
1456 (MO) and piriform cortex (PIR).

1457

1458 **Figure 7, Suppl. Table 1.**

1459 Definition of brain area abbreviations, and correspondence of the names across the Allen Brain
1460 Atlas and the Mouse Brain Atlas of Franklin and Paxinos (2016).

1461 **Figure 8, Figure Suppl. 1**

1462 (**A**) *Left* panel, example traces of paired-pulse ratio measurements at 50 ms inter-stimulus interval.
1463 Traces are from a $D1R^{Cre}$ and $Adora^{Cre}$ mouse (green and red traces, respectively). *Right*,
1464 quantification of the paired-pulse ratio from all recorded cells (n = 12 D1R+ and n = 18 Adora+
1465 AStria neurons).

1466 **(B)** Excitation-inhibition (E/I) ratio was measured by recording optogenetically-evoked EPSCs at -
1467 70 mV, and subsequently recording optogenetically-evoked IPSCs at the reversal potential for the
1468 EPSCs (+5 to +15 mV across experiments). *Left* panel shows example traces, the quantification of
1469 E/I ratio (*middle*), and the quantification of latency between the start of the light pulse and the
1470 respective PSC (*right*, for n = 12 D1R+ and n = 14 Adora+ AStria neurons). The statistical
1471 information for E/I ratios is given in the Results text. The delays for EPSCs were significantly
1472 shorter than the delays for IPSCs (D1R: $p = 0.001$, paired t-test; Adora: $p < 0.0001$, Wilcoxon
1473 matched-pairs signed-rank test). Data are shown as average ± SEM.

1474

1475 **Figure 8, Figure Suppl. 2**

1476 EPSC traces illustrating the measurement of paired-pulse ratios in a D1R+ neuron from a mouse
1477 that had undergone the "CS only" protocol (left), and in a D1R+ neuron from a mouse that had
1478 undergone the "CS+US" protocol. Relates to the dataset shown in Figure 8G.

1479

1480 **Figure 8, Figure Suppl. 3**

1481 EPSC traces illustrating the measurement of AMPA/NMDA ratios in a Adora+ neuron from a
1482 $Adora^{Cre}$ x Ai14 mouse that had undergone the "CS only" protocol (left), and in a Adora+ neuron
1483 from a $Adora^{Cre}$ x Ai14 mouse that had undergone the "CS+US" protocol. Relates to the dataset
1484 shown in Figure 8H.

1485

1486

1487 **Figure 8, Figure Suppl. 4**

1488 Anatomical evidence that D1R+ and Adora+ AStria neurons are analogous to striato-nigral, and
1489 striato-pallidal neurons of a direct, and indirect pathway, respectively. The images show slide
1490 scanner images of the fluorescence of eGFP, after bi-lateral injection of AAV1:CAG:FLEX:eGFP
1491 into the AStria of $D1R^{Cre}$ - and $Adora^{Cre}$ mice (B, C, respectively). Note that eGFP expression in
1492 D1R+ neurons of the AStria leads to axonal labelling in the GPe which we interpret as axons of
1493 passage, and to labeling in the GPi and SNR which is confined to the lateral parts of these nuclei.
1494 On the other hand, eGFP expression in Adora+ neurons of the AStria leads to labeling in the GPe.
1495 The experiments were taken from the control data sets of *in-vivo* optogenetic experiments of
1496 Figures 5, 6.

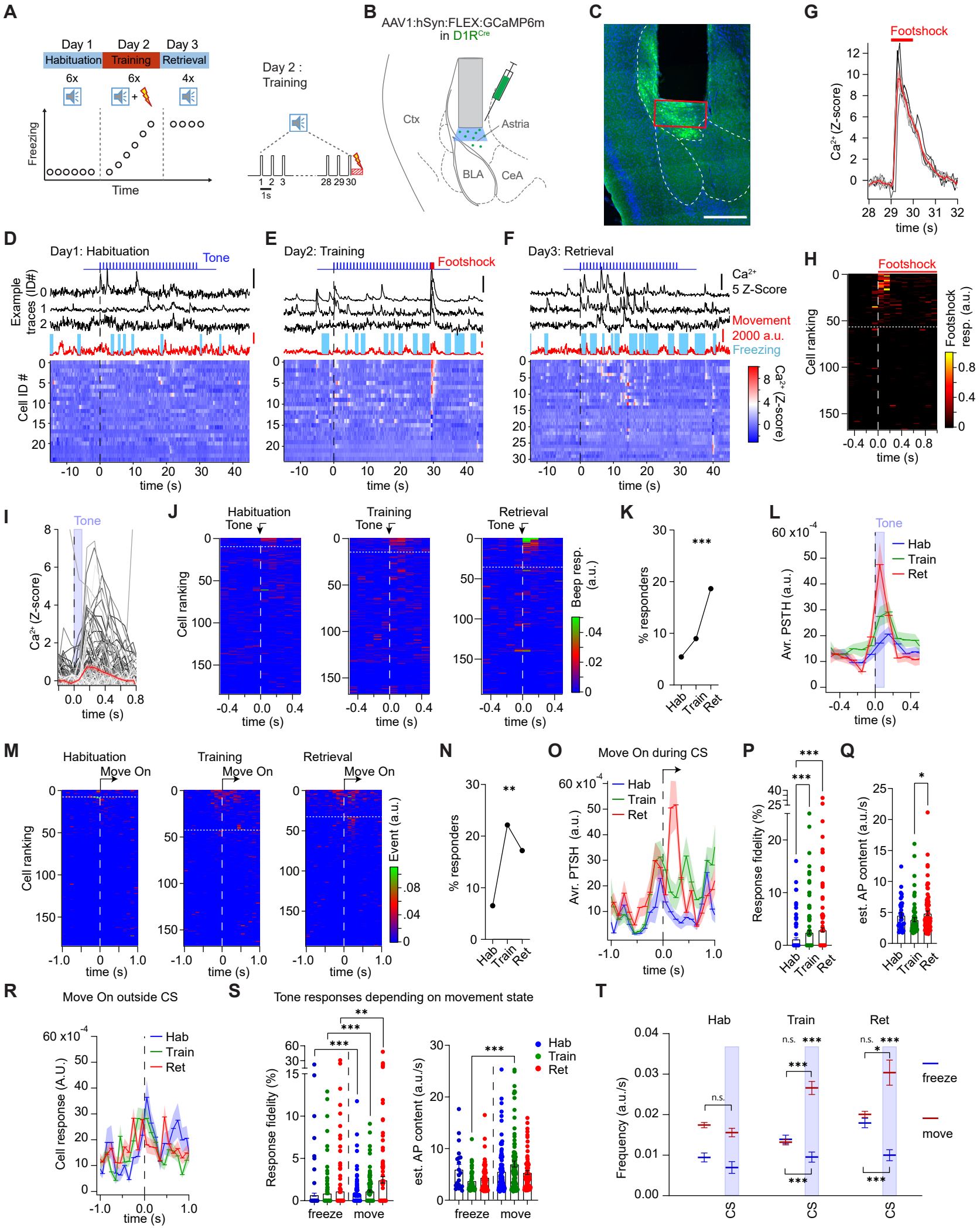
A
Day 1
Day 2
Day 3
Habituation
Training
Retrieval
6x
6x
4x
Freezing
Time
Day 2 :
Training
1 2 3
28 29 30
1s
B
AAV1:hSyn:FLEX:GCaMP6m
in D1R^Cre
Ctx
Astria
BLA
CeA
C
G
Footshock
Ca2+ (Z-score)
time (s)
D
Day1: Habituation
Tone
Example traces (ID#)
Cell ID #
time (s)
E
Day2: Training
Footshock
F
Day3: Retrieval
Ca2+
5 Z-Score
Movement
2000 a.u.
Freezing
Ca2+ (Z-score)
H
Footshock
Cell ranking
Footshock resp. (a.u.)
time (s)
I
Tone
Ca2+ (Z-score)
time (s)
J
Habituation
Training
Retrieval
Tone
Cell ranking
Beep resp. (a.u.)
time (s)
K
***
% responders
Hab
Train
Ret
L
Tone
Hab
Train
Ret
Avr. PSTH (a.u.)
time (s)
M
Habituation
Training
Retrieval
Move On
Cell ranking
Event (a.u.)
time (s)
N
**
% responders
Hab
Train
Ret
O
Move On during CS
Hab
Train
Ret
Avr. PTSH (a.u.)
time (s)
P
***
***
Response fidelity (%)
Hab
Train
Ret
Q
*
est. AP content (a.u./s)
Hab
Train
Ret
R
Move On outside CS
Hab
Train
Ret
Cell response (A.U.)
time (s)
S
Tone responses depending on movement state
**
***
***
Response fidelity (%)
freeze
move
***
Hab
Train
Ret
est. AP content (a.u./s)
freeze
move
T
Hab
Train
Ret
n.s.
n.s.
***
n.s.
***
*
***
***
***
Frequency (a.u./s)
freeze
move
CS
CS
CS

Figure 1

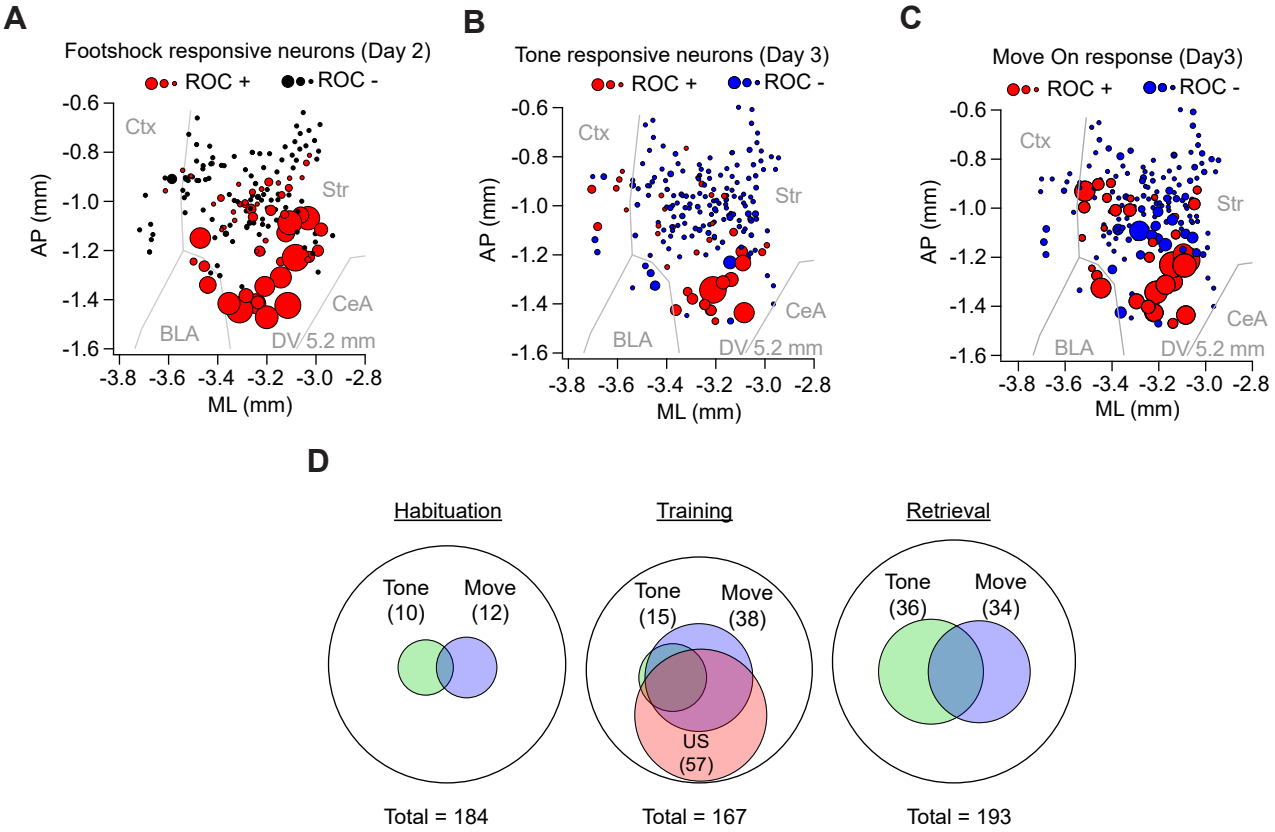
A
Footshock responsive neurons (Day 2)
ROC +
ROC -
Ctx
Str
CeA
BLA
DV/5.2 mm
AP (mm)
ML (mm)
B
Tone responsive neurons (Day 3)
ROC +
ROC -
C
Move On response (Day3)
ROC +
ROC -
D
Habituation
Training
Retrieval
Tone (10)
Move (12)
Tone (15)
Move (38)
US (57)
Tone (36)
Move (34)
Total = 184
Total = 167
Total = 193

Figure 2

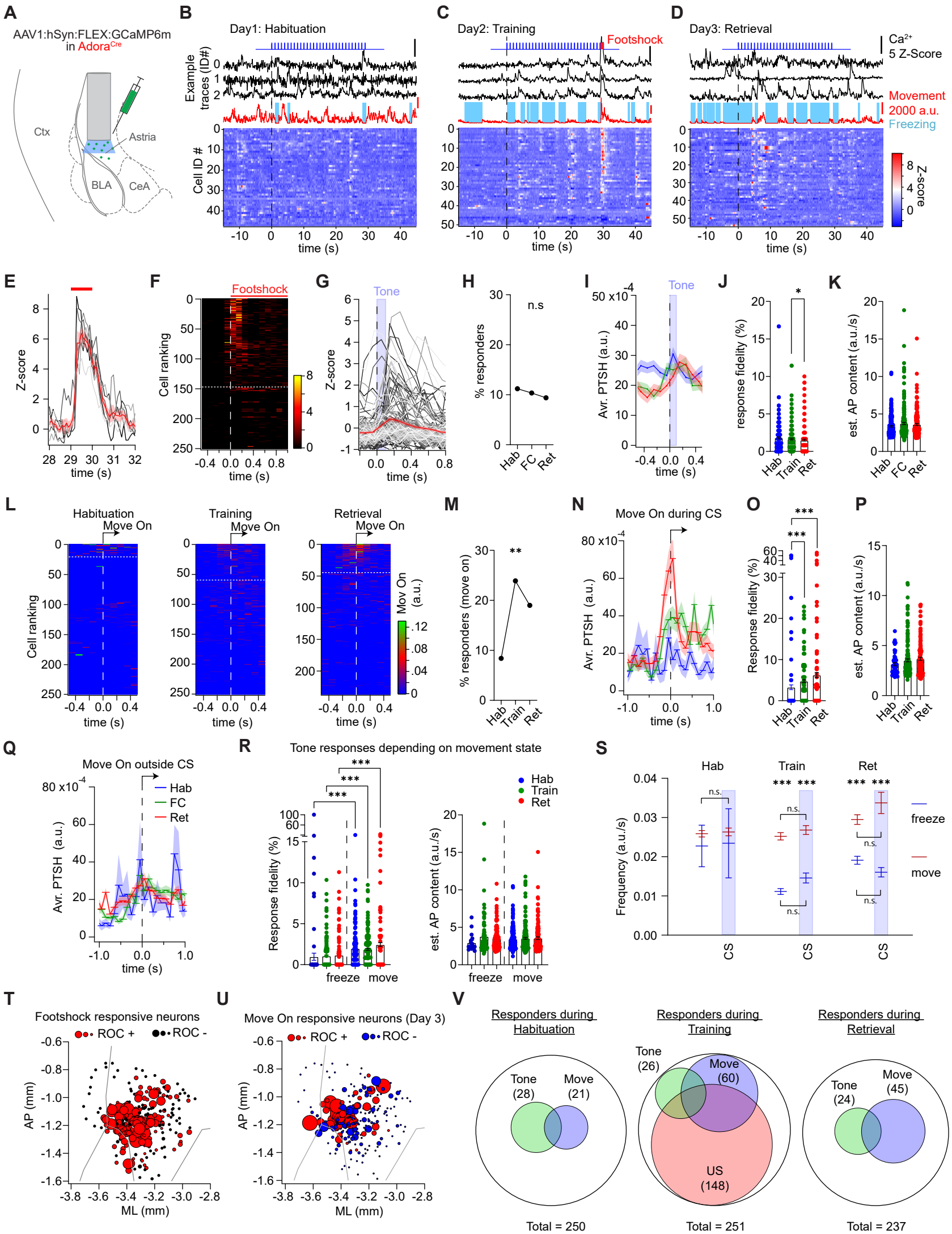
A
AAV1:hSyn:FLEX:GCaMP6m in Adora^Cre
Ctx
Astria
BLA
CeA
B
Day1: Habituation
Example traces (ID#)
Cell ID #
time (s)
C
Day2: Training
Footshock
D
Day3: Retrieval
Ca2+
5 Z-Score
Movement
2000 a.u.
Freezing
Z-score
E
Z-score
time (s)
F
Footshock
Cell ranking
G
Tone
H
% responders
n.s
Hab
FC
Ret
I
Tone
Avr. PTSH (a.u.)
J
response fidelity (%)
K
est. AP content (a.u./s)
L
Habituation
Training
Retrieval
Move On
Mov On (a.u.)
M
% responders (move on)
N
Move On during CS
O
Response fidelity (%)
P
Q
Move On outside CS
R
Tone responses depending on movement state
freeze
move
S
Frequency (a.u./s)
CS
freeze
move
T
Footshock responsive neurons
ROC +
ROC -
AP (mm)
ML (mm)
U
Move On responsive neurons (Day 3)
V
Responders during Habituation
Tone (28)
Move (21)
Total = 250
Responders during Training
Tone (26)
Move (60)
US (148)
Total = 251
Responders during Retrieval
Tone (24)
Move (45)
Total = 237

Figure 3

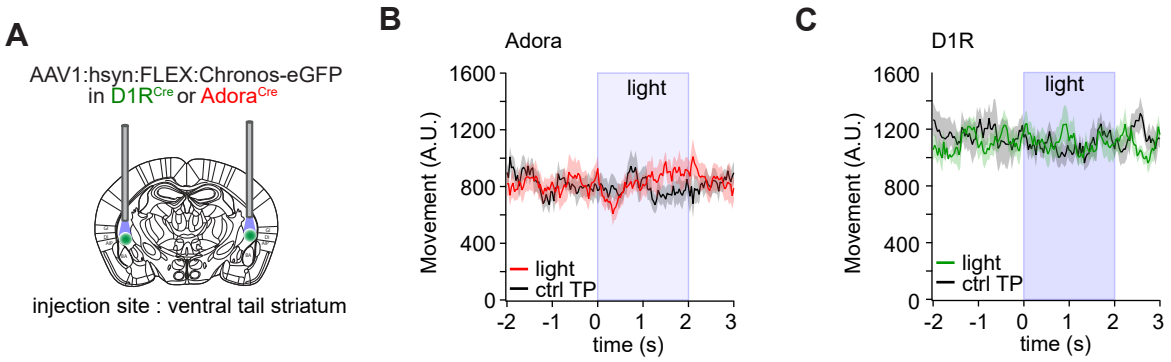
A
AAV1:hsyn:FLEX:Chronos-eGFP
in D1R^Cre or Adora^Cre
injection site : ventral tail striatum
B
Adora
light
Movement (A.U.)
1600
1200
800
400
0
light
ctrl TP
-2
-1
0
1
2
3
time (s)
C
D1R
light
Movement (A.U.)
1600
1200
800
400
0
light
ctrl TP
-2
-1
0
1
2
3
time (s)

Figure 4

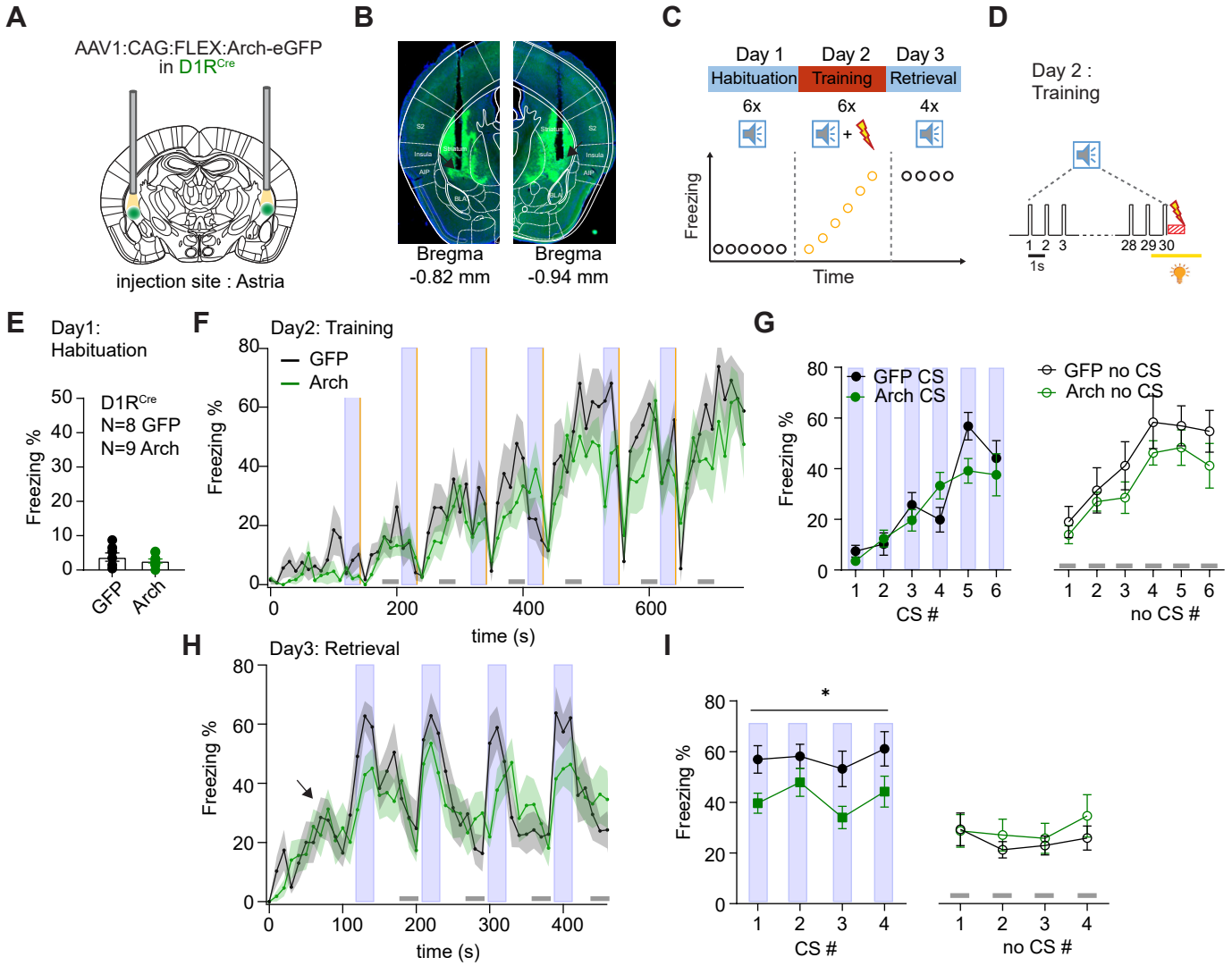
A
AAV1:CAG:FLEX:Arch-eGFP
in D1R^Cre
injection site : Astria
B
Bregma
-0.82 mm
Bregma
-0.94 mm
C
Day 1
Habituation
Day 2
Training
Day 3
Retrieval
6x
6x
4x
Freezing
Time
D
Day 2 :
Training
1 2 3
28 29 30
1s
E
Day1:
Habituation
D1R^Cre
N=8 GFP
N=9 Arch
Freezing %
GFP
Arch
F
Day2: Training
GFP
Arch
Freezing %
time (s)
G
GFP CS
Arch CS
GFP no CS
Arch no CS
Freezing %
CS #
no CS #
H
Day3: Retrieval
Freezing %
time (s)
I
*
Freezing %
CS #
no CS #

Figure 5

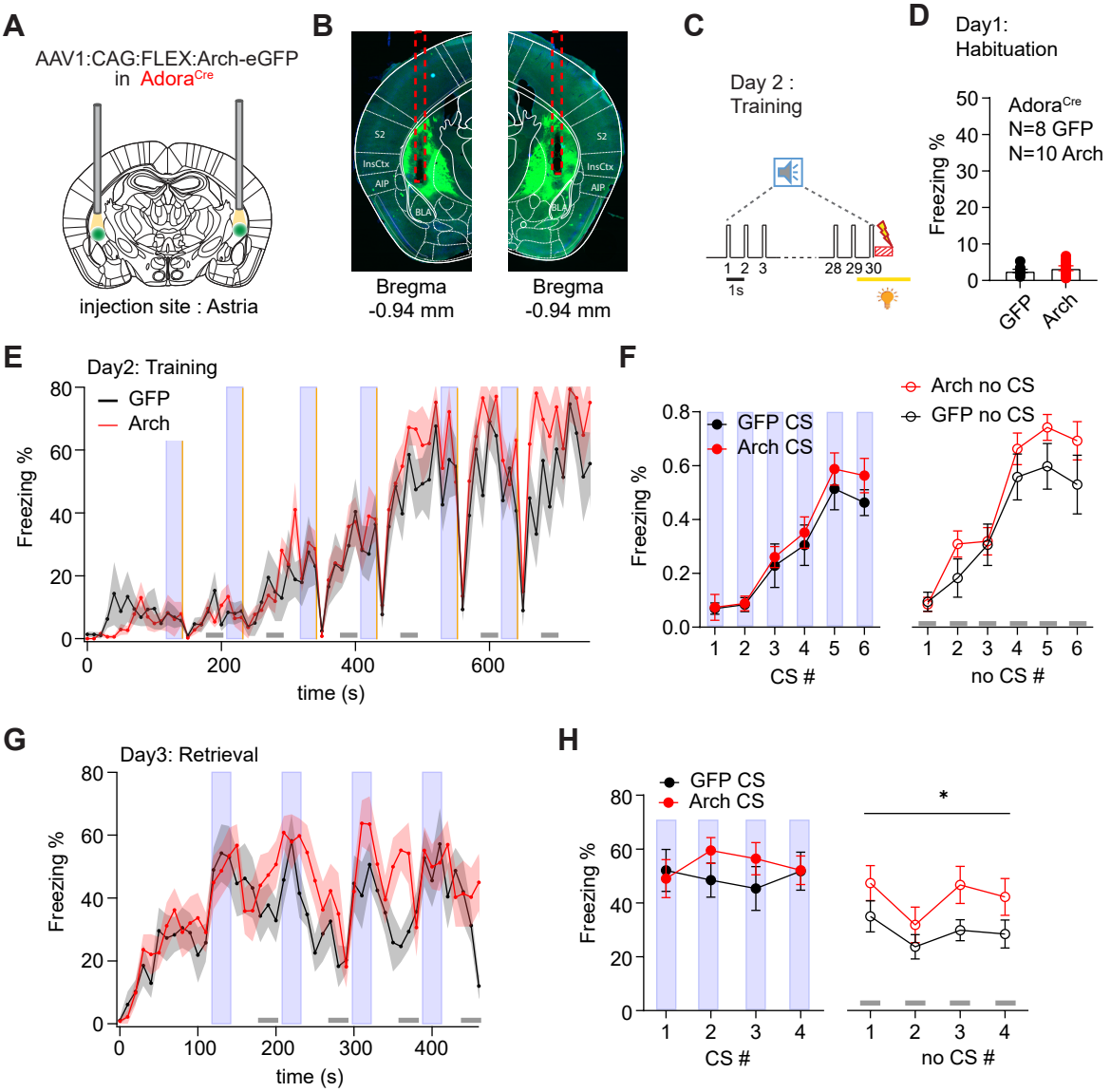
A
AAV1:CAG:FLEX:Arch-eGFP
in AdoraCre
injection site : Astria
B
S2
InsCtx
AIP
BLA
Bregma
-0.94 mm
Bregma
-0.94 mm
C
Day 2 :
Training
1 2 3
28 29 30
1s
D
Day1:
Habituation
AdoraCre
N=8 GFP
N=10 Arch
Freezing %
GFP
Arch
E
Day2: Training
GFP
Arch
Freezing %
time (s)
F
GFP CS
Arch CS
Arch no CS
GFP no CS
Freezing %
CS #
no CS #
G
Day3: Retrieval
Freezing %
time (s)
H
GFP CS
Arch CS
Freezing %
CS #
no CS #
*

Figure 6

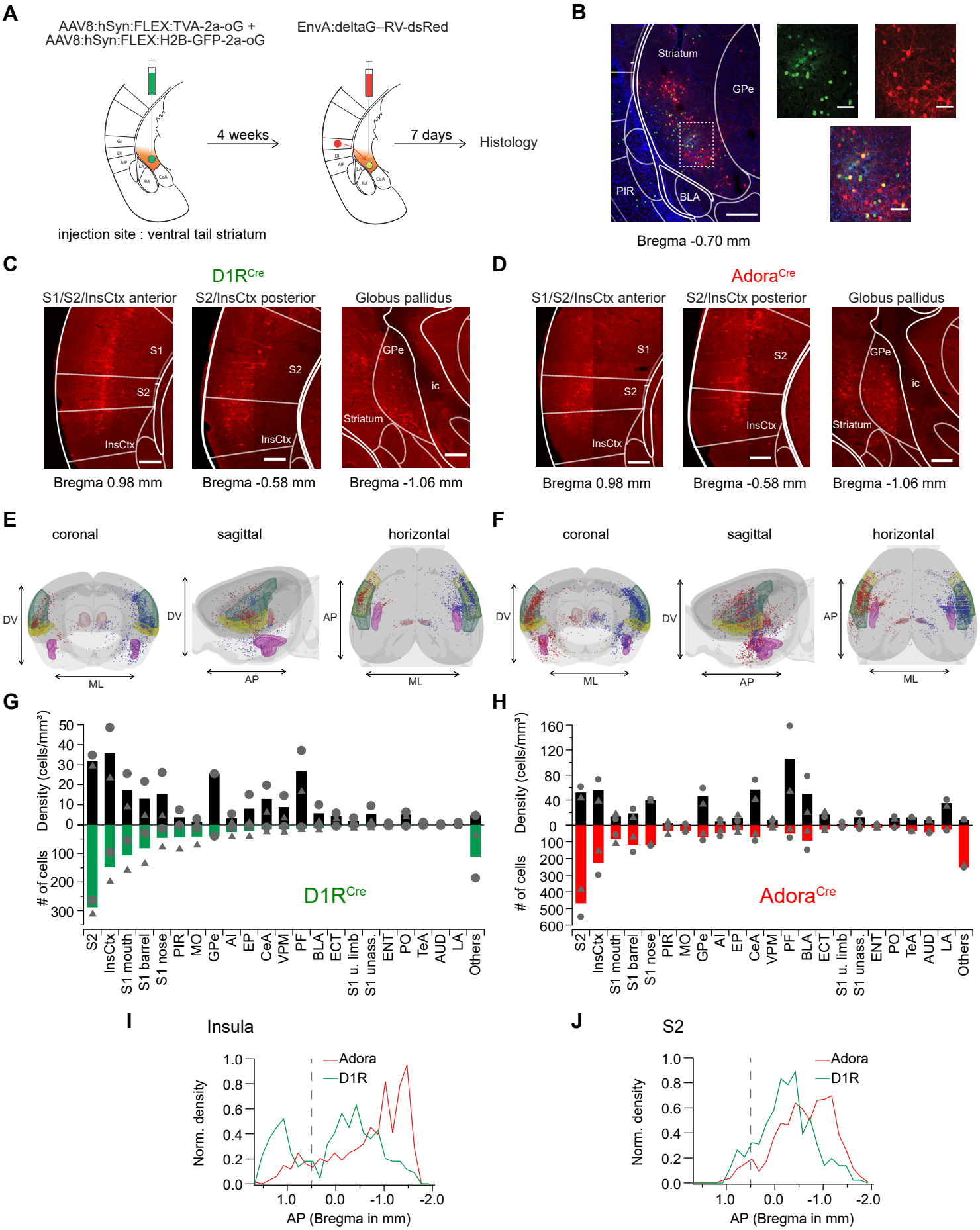
A
AAV8:hSyn:FLEX:TVA-2a-oG +
AAV8:hSyn:FLEX:H2B-GFP-2a-oG
EnvA:deltaG–RV-dsRed
4 weeks
7 days
Histology
injection site : ventral tail striatum
B
Striatum
GPe
PIR
BLA
Bregma -0.70 mm
C
D1R^Cre
S1/S2/InsCtx anterior
S2/InsCtx posterior
Globus pallidus
S1
S2
InsCtx
GPe
ic
Striatum
Bregma 0.98 mm
Bregma -0.58 mm
Bregma -1.06 mm
D
Adora^Cre
E
coronal
sagittal
horizontal
DV
ML
AP
F
G
Density (cells/mm³)
# of cells
D1R^Cre
S2
InsCtx
S1 mouth
S1 barrel
S1 nose
PIR
MO
GPe
AI
EP
CeA
VPM
PF
BLA
ECT
S1 u. limb
S1 unass.
ENT
PO
TeA
AUD
LA
Others
H
Adora^Cre
I
Insula
Adora
D1R
Norm. density
AP (Bregma in mm)
J
S2

Figure 7

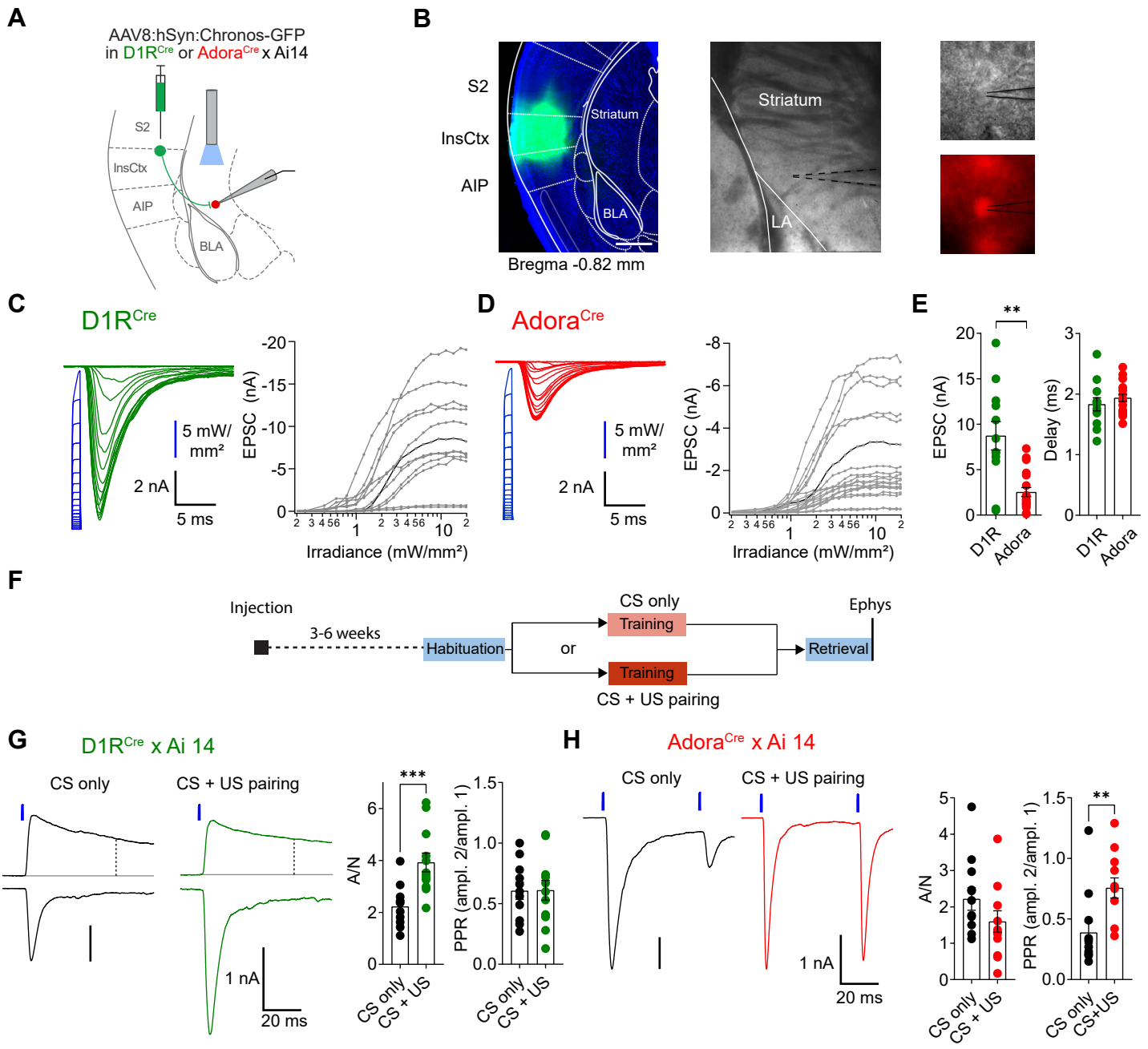
A
AAV8:hSyn:Chronos-GFP
in D1R^Cre or Adora^Cre x Ai14
S2
InsCtx
AIP
BLA
B
S2
InsCtx
AIP
Striatum
BLA
Bregma -0.82 mm
Striatum
LA
C
D1R^Cre
5 mW/ mm²
2 nA
5 ms
EPSC (nA)
Irradiance (mW/mm²)
D
Adora^Cre
5 mW/ mm²
2 nA
5 ms
EPSC (nA)
Irradiance (mW/mm²)
E
**
EPSC (nA)
Delay (ms)
D1R
Adora
F
Injection
3-6 weeks
Habituation
or
CS only
Training
Training
CS + US pairing
Ephys
Retrieval
G
D1R^Cre x Ai 14
CS only
CS + US pairing
1 nA
20 ms
***
A/N
PPR (ampl. 2/ampl. 1)
CS only
CS + US
H
Adora^Cre x Ai 14
CS only
CS + US pairing
1 nA
20 ms
**
A/N
PPR (ampl. 2/ampl. 1)
CS only
CS+US

Figure 8

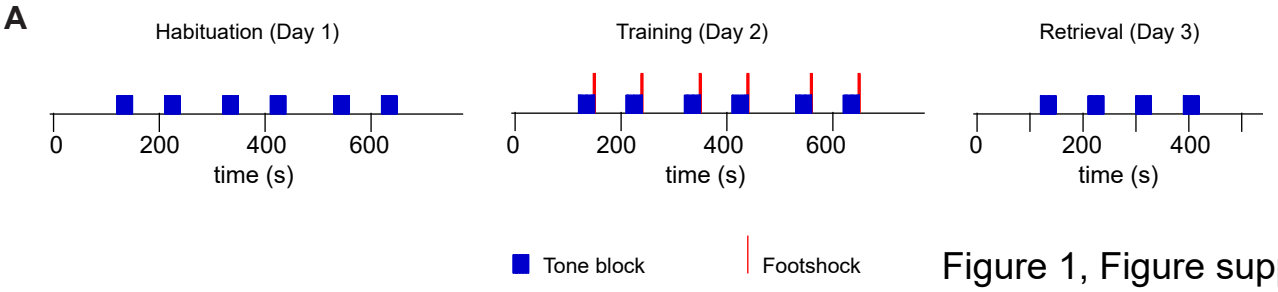

Figure 1, Figure suppl. 1

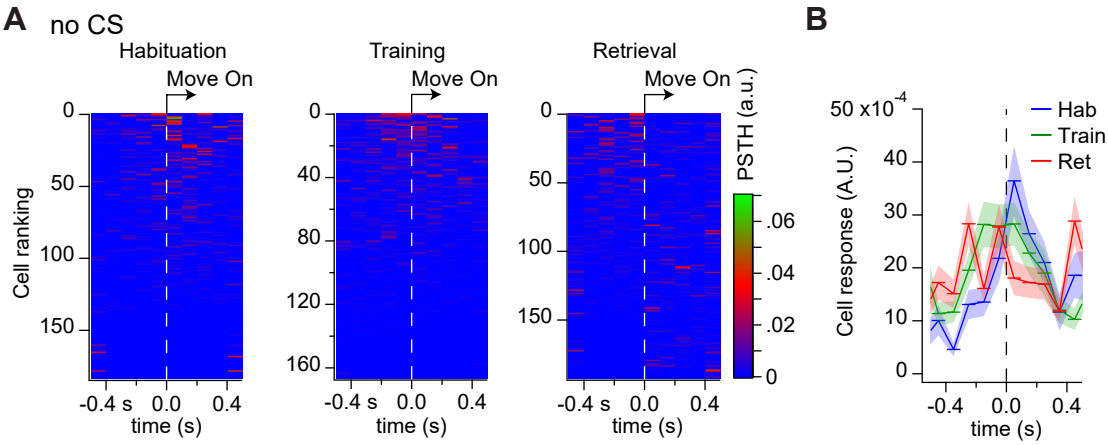

Figure 1, Figure suppl. 2

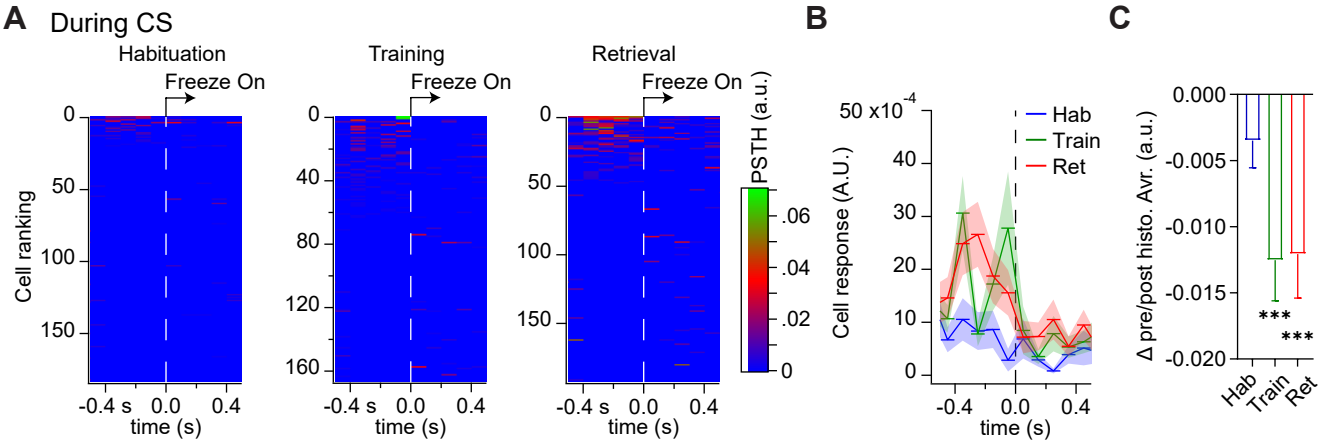

Figure 1, Figure suppl. 3

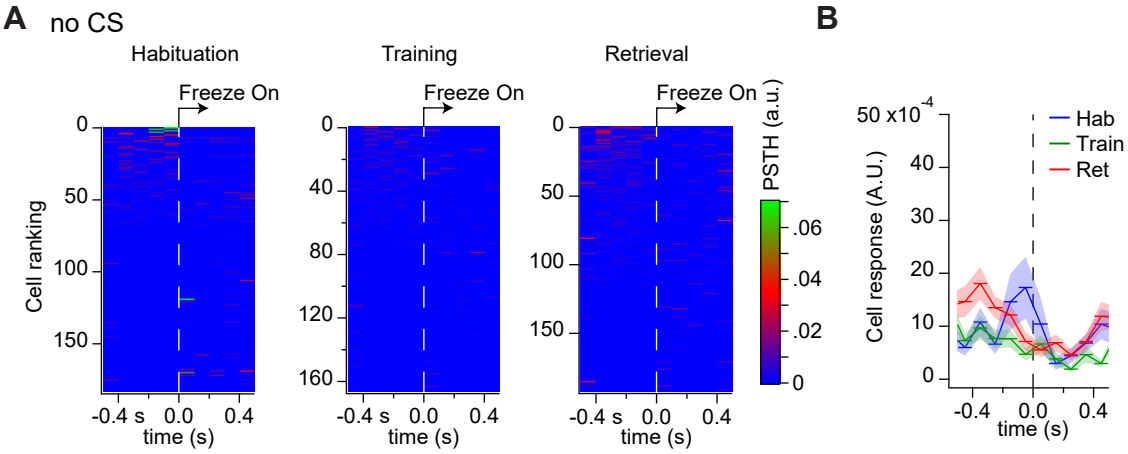

Figure 1, Figure suppl. 4

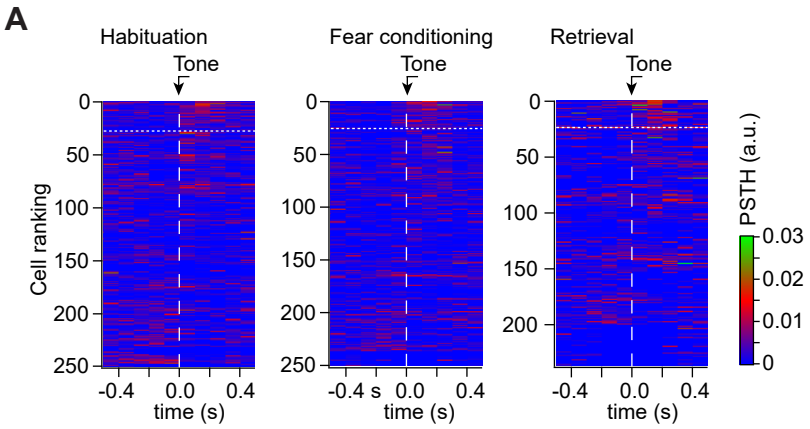

Figure 3, Figure suppl. 1

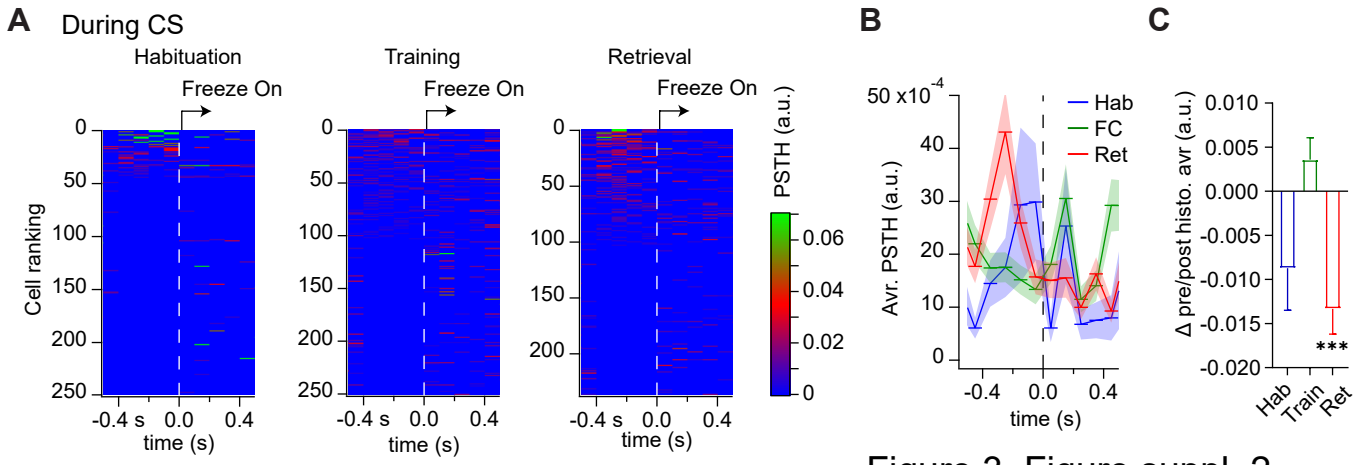

Figure 3, Figure suppl. 2

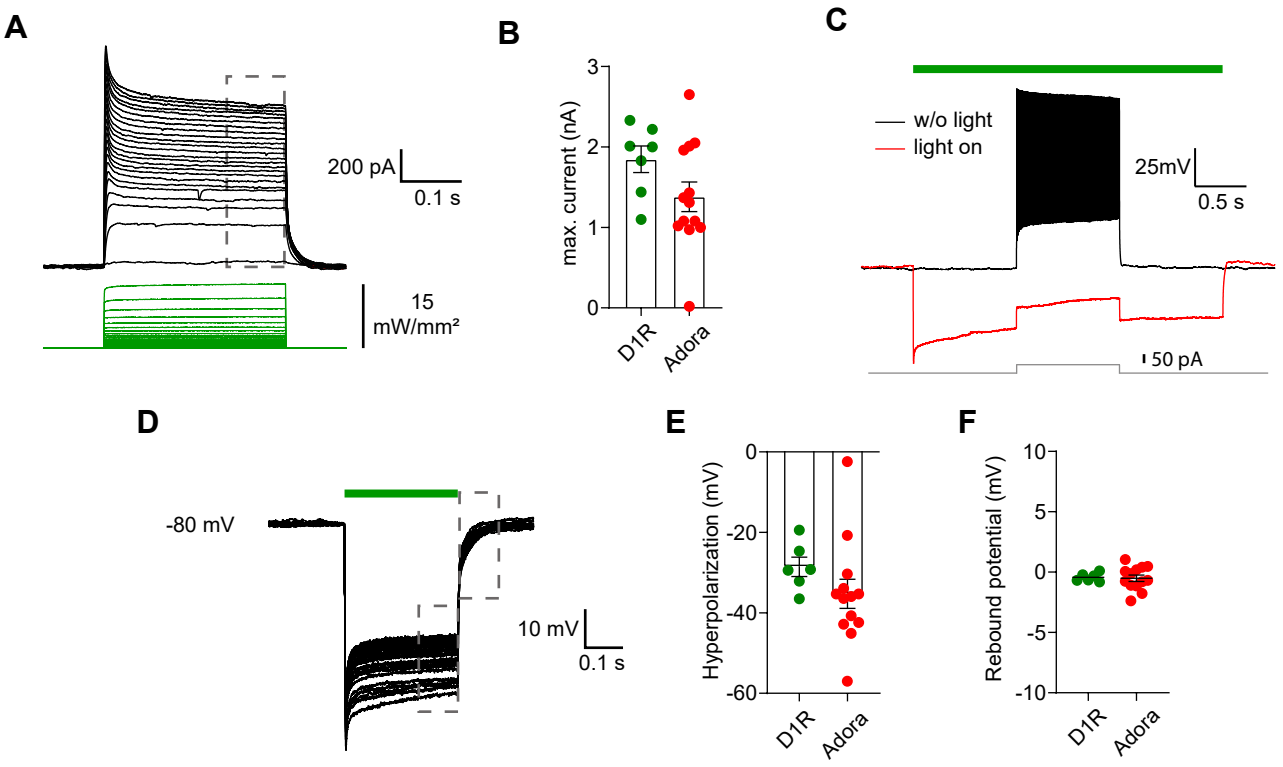

Figure 5, Figure suppl. 1

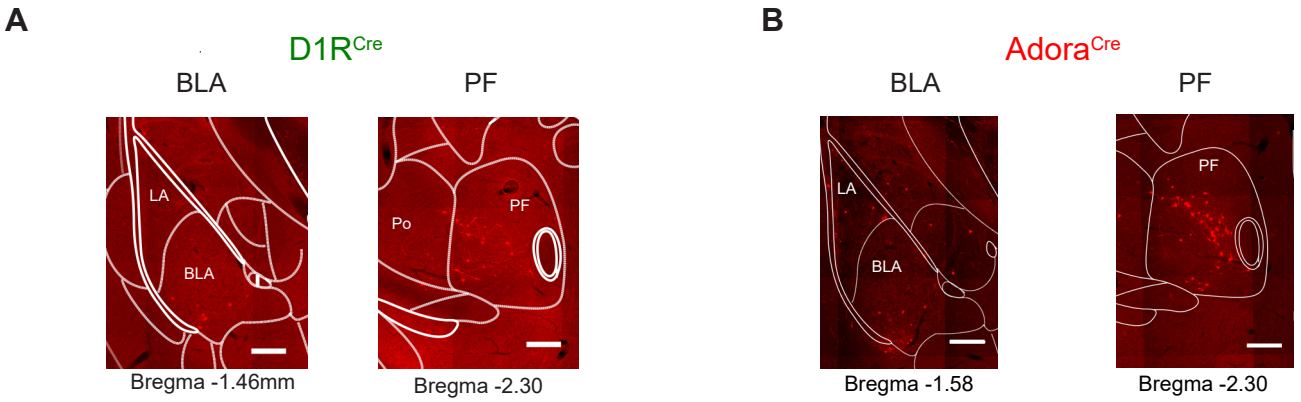

Figure 7, Figure suppl. 1

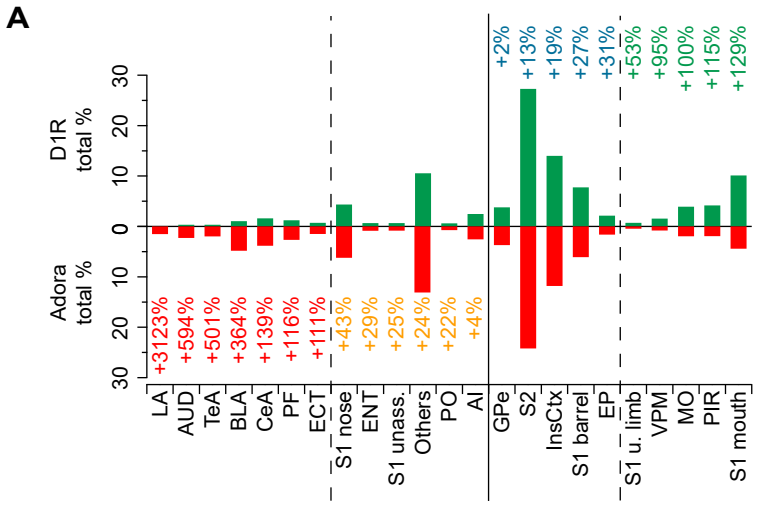

Figure 7, Figure suppl. 2

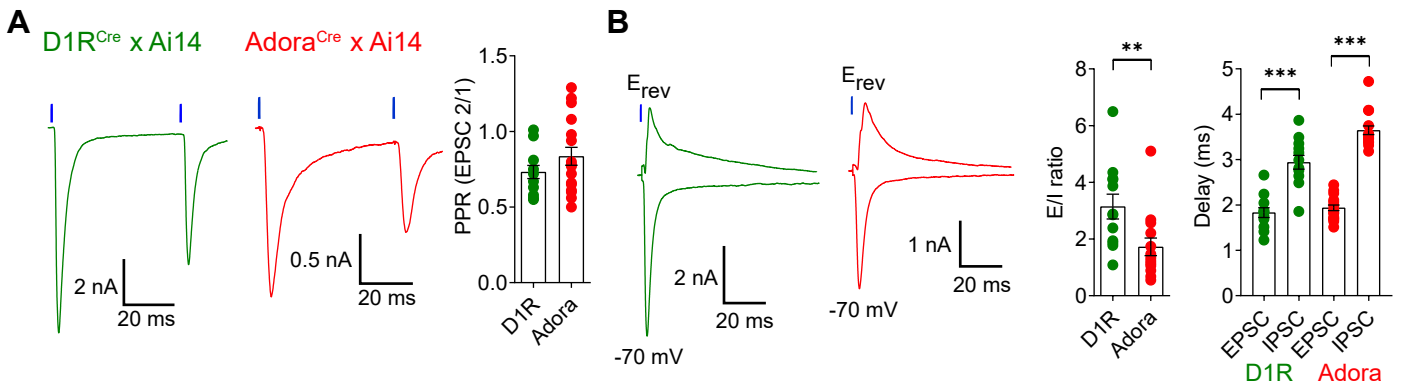

Figure 8, Figure Suppl. 1

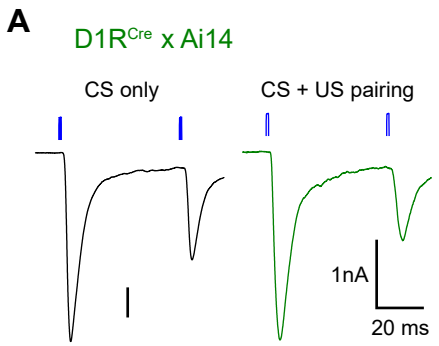

Figure 8, Figure Suppl. 2

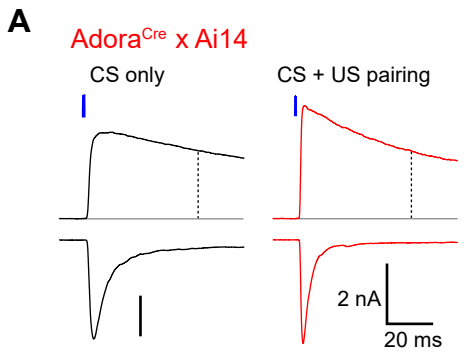

Figure 8, Figure Suppl. 3

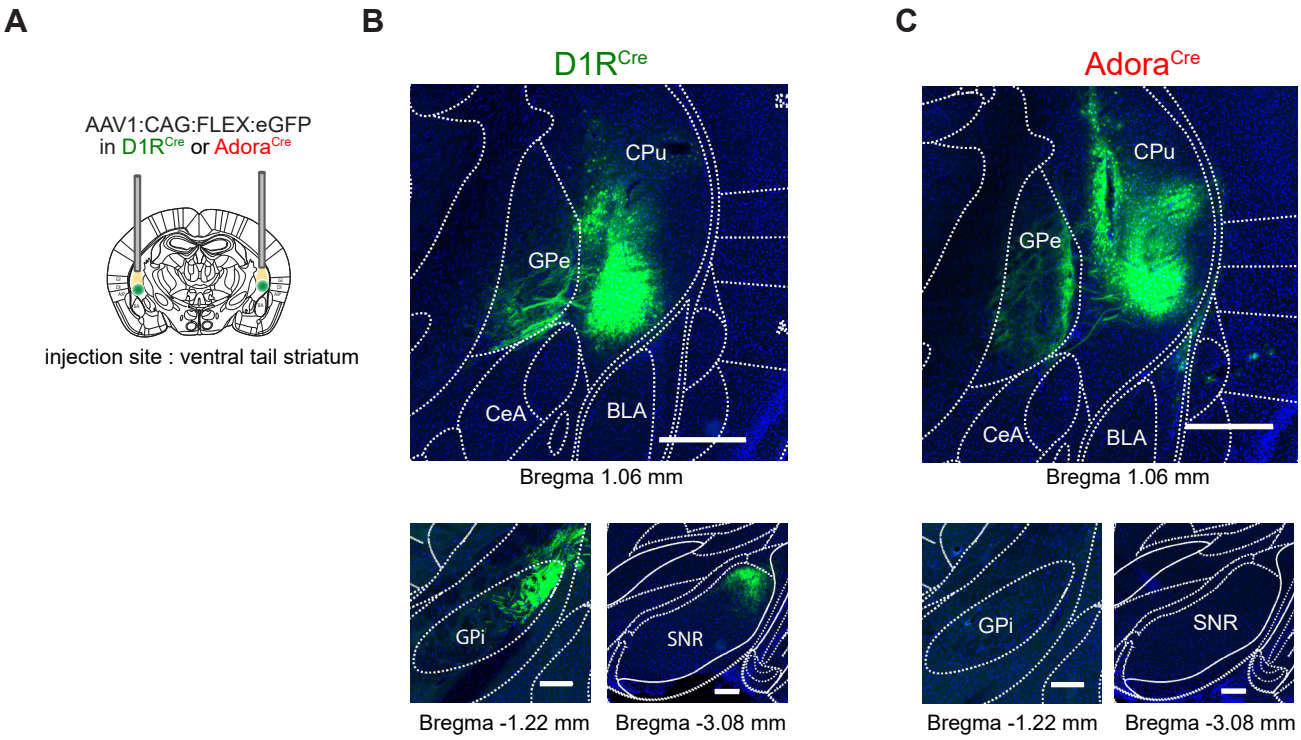

Figure 8, Figure suppl. 4

Figure 7, Suppl.Table 1

Abbreviation	Allen Brain atlas	Franklin and Paxinos
AI	Agranular insular area	Agranular insular cortex (dorsal, ventral and posterior)
AUD	Auditory areas (dorsal and ventral)	Auditory cortex (dorsal, primary and ventral)
BLA	Basolateral amygdalar nucleus (anterior, posterior and ventral)	Basolateral amygdaloid nucleus (anterior, posterior)
CeA	Central amygdalar nucleus (capsular, medial and lateral)	Central amygdaloid nucleus (capsular, medial and lateral)
Ect	Ectorhinal area	Ectorhinal cortex
ENT	Entorhinal area	Entorhinal cortex
EP	Endopiriform nucleus	Claustrum (dorsal, ventral and endopiriform)
GPe	Globus pallidus, external segment	Globus pallidus
GPi	Globus pallidus, internal segment	Entopenduncular nucleus
InsCtx	Gustatory areas and Visceral area	Insular cortex (granular and dysgranular)
LA	Lateral amygdalar nucleus	Lateral amygdaloid nucleus
MO	Primary motor area	Primary motor cortex
PF	Parafascicular nucleus	Parafascicular thalamic nucleus
PIR	Piriform area	Piriform cortex
PO	Posterior complex of the thalamus	Posterior thalamic nuclear group
S1 barrel	Primary somatosensory area, barrel field	Primary somatosensory cortex, barrel field
S1 mouth	Primary somatosensory area, mouth	Primary somatosensory cortex, upper lip/barrel field
S1 nose	Primary somatosensory area, nose	Primary somatosensory cortex, upper lip
S1 unassigned	Primary somatosensory area, unassigned	Primary somatosensory cortex, dysgranular zone
S1 upper limb	Primary somatosensory area, upper limb	Primary somatosensory cortex, shoulder region
S2	Supplemental somatosensory area	Secondary somatosensory cortex
SNR	Substantia nigra, reticular part	Substantia nigra, reticular part
TeA	Temporal association areas	Temporal association cortex
VPM	Ventral posteromedial nucleus of the thalamus	Ventral posteromedial thalamic nucleus